Acta Pharmaceutica Sinica B 2025;15(8):4265−4284

Chinese Pharmaceutical Association
Institute of Materia Medica, Chinese Academy of Medical Sciences

Acta Pharmaceutica Sinica B

www.elsevier.com/locate/apsb
www.sciencedirect.com

ORIGINAL ARTICLE

Unveiling the renoprotective mechanisms of self-assembled herbal nanoparticles from *Scutellaria barbata* and *Scleromitrion diffusum* in acute kidney injury: A nano-TCM approach

Lunyue Xia[a,†], Qunfang Yang[b,†], Kangzhe Fu[a], Yutong Yang[a], Kaiyue Ding[a], Yuexue Huo[a], Lanfang Zhang[b], Yunong Li[b], Borong Zhu[b], Peiyu Li[a], Yijie Huo[a], Liang Sun[c], Ya Liu[b], Haigang Zhang[b], Tao Liu[b,*], Wenjun Shan[b,*], Lin Zhang[a,*]

[a]*Institute of Integrative Medicine, Dalian Medical University, Dalian 116000, China*
[b]*Department of Pharmacology, College of Pharmacy and Laboratory Medicine, Army Medical University (Third Military Medical University), Chongqing 400038, China*
[c]*Shenzhen Research Institute, City University of Hong Kong, Shenzhen 518000, China*

Received 12 January 2025; received in revised form 10 April 2025; accepted 22 May 2025

KEY WORDS

Nano-TCM;
Self-assemble;
Protein corona;
SSNPs;
AKI;
Nrf2;
Ferroptosis

Abstract Acute kidney injury (AKI) is a critical clinical condition characterized by rapid renal function decline, with high morbidity, mortality, and healthcare costs. Traditional Chinese medicine (TCM) has shown potential effects on mitigating oxidative stress and programmed cell death in AKI models. *Scutellaria barbata* D. Don (SB) and *Scleromitrion diffusum* (Willd.) R. J. Wang (SD), a classic TCM herbal pair exhibited anti-inflammatory and antioxidant activities. Using advanced chromatographic separation technology, we enriched the effective fractions of water extracts from SB−SD, obtaining self-assembled herbal nanoparticles (SB and SD nanoparticles, SSNPs) rich in flavonoids and terpenoids. These SSNPs demonstrated robust antioxidant properties *in vitro* and mitigated AKI progression *in vivo* by activating the nuclear factor erythroid 2-related factor 2 (Nrf2) signaling pathway. Oral administration of SSNPs in mice resulted in absorption into the bloodstream, formation of a protein corona, reduced macrophage phagocytosis, and enhanced bioavailability and renal targeting. Furthermore, we investigated the self-assembly principle of SSNPs using representative flavonoids and terpenoids. Kinetic

*Corresponding authors.
E-mail addresses: liutao@tmmu.edu.cn (Tao Liu), wjshan@tmmu.edu.cn (Wenjun Shan), linzhang@dmu.edu.cn (Lin Zhang).
[†]These authors made equal contributions to this work.

Peer review under the responsibility of Chinese Pharmaceutical Association and Institute of Materia Medica, Chinese Academy of Medical Sciences.

https://doi.org/10.1016/j.apsb.2025.05.024

studies and *in situ* transmission electron microscopy (*in situ* TEM) revealed that these compounds self-assemble *via* supramolecular forces like hydrogen bonding and $\pi-\pi$ interactions, forming stable nanostructures. This study elucidates the renoprotective effects and mechanisms of SB and SD, and provides a novel approach for the development of TCM-based nanomedicines, highlighting the potential of nano-TCM in AKI treatment.

1. Introduction

Acute kidney injury (AKI), characterized by a sudden deterioration of renal function over a short period, is a common complication with high morbidity and mortality as well as a substantial expenses to healthcare systems[1,2]. Clinically, diverse etiologies, such as cisplatin (DDP) nephrotoxicity, ischemia, sepsis or urinary tract obstruction, lead to heterogeneous AKI pathogenesis which serves as a considerable impediment to its treatment[3,4]. Emerging evidence suggests that oxidative stress connecting ferroptosis and inflammation responses associated with excessive accumulation of reactive oxygen species (ROS) and lipid metabolism may represent a common pathophysiological process of various types of AKI[5,6]. Therefore, pharmacological agents that possess anti-oxidative, anti-ferroptosis and anti-inflammatory properties may be an imperative therapeutic strategy for AKI.

Numerous studies have indicated that herbal medicines, especially traditional Chinese medicine (TCM) exhibited high efficacy in inhibiting oxidative stress[7,8], programmed cell death and inflammatory responses, which have been extensively tested in animal models of AKI and even in patients[9,10]. *Scutellaria barbata* D. Don (SB) and *Scleromitrion diffusum* (Willd.) R. J. Wang (SD), as a classic herbal pair for clearing heat and detoxifying, have not only a long history of application in cancer treatment, but also exhibit multiple pharmacological activities such as anti-inflammation and antioxidation, showing good therapeutic effects for various diseases[11,12]. These two herbs are abundant in resources worldwide and are an important treasure of the natural medicine system. However, whether SB−SD herbal pair exert renal protective effects and the underlying mechanism is currently unclear.

It is well known that TCM decoction, the oldest and most common traditional form of herbal preparation, uses water as a solvent to prepare single or multiple herbal slices by boiling, with a long history of treating diseases and widely used in clinical practice due to its high concentration, easy to take and absorb. Notwithstanding the great potential, the initial decoction of TCM still faces many challenges in effective component enrichment, component analysis, and unclear therapeutic material basis. Given the remarkable advances in the cross-integration of nanoscience and TCM research, TCM decoction contains not only water-soluble components, but also a large number of nano-scale small particles, which means that TCM decoction is actually a complex multi-phase dispersion system containing supramolecular aggregates[13,14]. The formation of these supramolecular aggregates is mainly due to the interaction between various chemical components and the self-assembly process during the decoction process[15,16]. Studies have shown that supramolecular aggregates in TCM decoctions can significantly improve the solubility and stability of the active ingredients and promote their absorption in the gastrointestinal tract, thereby demonstrating superior pharmacodynamic activities[17]. These findings provide a new perspective and way to reveal the material basis of TCM and elucidate its mechanism of action.

Based on the aforementioned considerations, we utilized an advanced chromatographic separation technology to accurately enrich the effective fractions of water extracts of *Scutellaria barbata* (SB) and *Scleromitrion diffusum* (SD) and the active fraction (SB and SD nanoparticles, SSNPs) with flavonoids and terpenoids as the main components were successfully obtained. The final SSNPs are able to self-assemble into supramolecular aggregates, which exhibit particularly robust antioxidant properties *in vitro* and exert anti-oxidative, anti-ferroptotic and anti-inflammatory effects to ameliorate AKI progression *via* activating nuclear factor erythroid 2-related factor 2 (Nrf2) signaling pathway. Moreover, after oral administration in mice, these effective ingredient nanoparticles can be absorbed into the blood in the intestines and form protein corona on their surface, effectively reducing the phagocytosis of macrophages and improving the bioavailability and special renal-targeting capacity (Scheme 1).

To go a step further, we try to probe the principle of self-assembly observed here and to explore whether this molecular self-assembly principle is adaptable for the application of nano-TCM. Scutellarin (STR) and geniposidic acid (GPA) were selected as two representative flavonoids and terpenoids, we conducted preliminary kinetic studies on both two-component reactions and employed *in situ* electron microscopy, the results demonstrated that two representative components can achieve self-assembly *via* supramolecular forces such as hydrogen bonding and $\pi-\pi$ interactions, thereby forming stable nanostructures. Overall, this study not only elucidated the specific renoprotective effects and underlying mechanisms of *Scutellaria barbata* and *Scleromitrion diffusum*, but also offered a novel approach and methodology for the research and development of TCM and nano-TCM.

2. Materials and methods

2.1. Materials

Scutellaria barbata D. Don (SB) and *Scleromitrion Diffusum* (Willd.) R. J. Wang (SD) were purchased from Beijing Tong Ren Tang Co., Ltd. (Beijing, China). Scutellarin and geniposidic acid were purchased from Chemxyz Biotech Co., Ltd. (Shanghai, China). ML385, DDP, 2′,7′-dichlorodihydrofluorescein diacetate (H2DCFDA), Cyanine5.5 (Cy5.5) and FITC were purchased from MedChemExpress Co., Ltd. (NJ, USA). C11-BODIPY$^{581/591}$, Mitotracker™ Green, Mitotracker™ Deep Red and MitoSOX™ Red were purchased from Thermo Fisher Technology Co., Ltd.

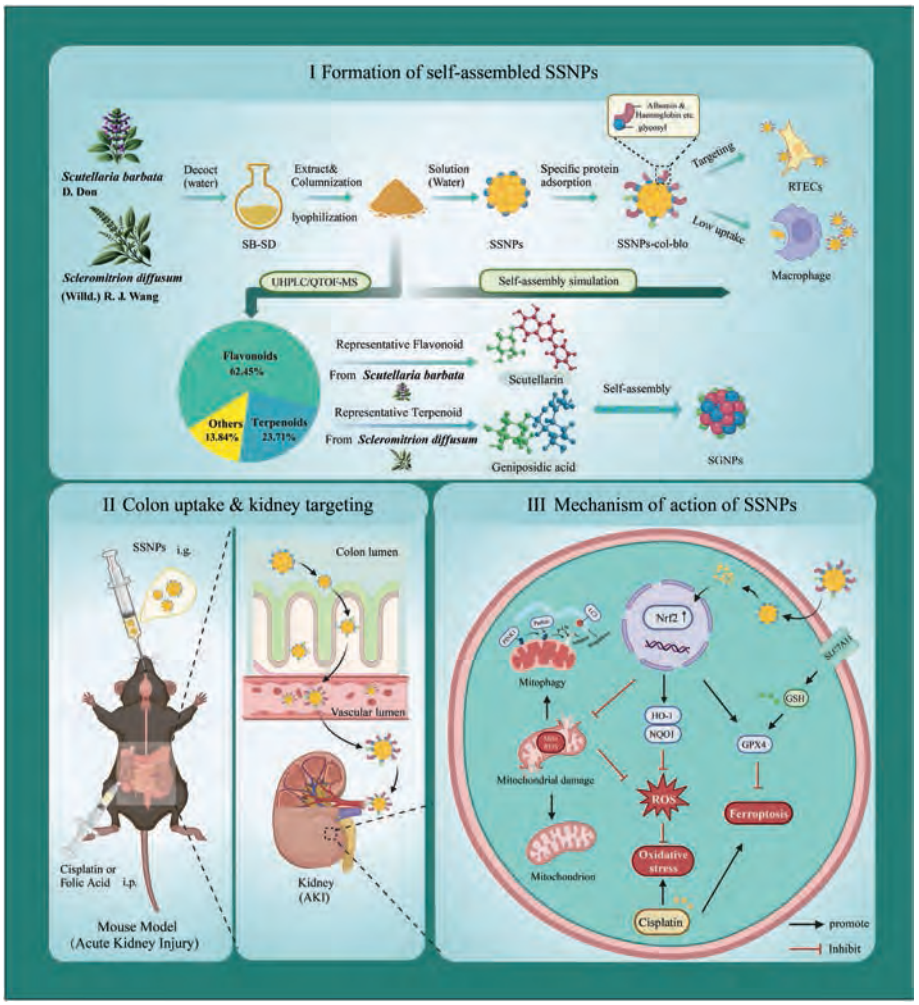

Scheme 1 Schematic illustration of a nano-TCM strategy for investigating the mechanisms underlying the renoprotective effects of the self-assembled herbal nanoparticles (SSNPs) derived from *Scutellaria barbata* D. Don (SB) and *Scleromitrion diffusum* (Willd.) R. J. Wang (SD) on cisplatin (DDP)- and folic acid (FA)-induced kidney injury.

(Shanghai, China). Mitochondrial membrane potential assay kit (JC-10) was purchased from Biosharp biotechnology Co., Ltd. (Hefei, China). Malondialdehyde (MDA) assay kit, reduced glutathione (GSH) assay kit, blood urea nitrogen (BUN) assay kit and blood creatinine (CRE) assay kit were purchased from Nanjing Jiancheng Bioengineering Institute (Nanjing, China). Fast silver stain kit and cell counting kit-8 (CCK-8) were provided by Beyotime Institute of Biotechnology (Shanghai, China). Intracellular iron colorimetric assay kit was purchased from Applygen Technology Co., Ltd. (Beijing, China). The following primary antibodies were used: anti-Nrf2 (Proteintech, 16396-1-AP, China), anti-NQO1 (ABclonal, A23486, China), anti-HO-1 (Abcam, ab52947, UK), anti-GPX4 (Zenbio, R381958, China), anti-xCT (Zenbio, R26116, China), anti-4-HNE (ABclonal, A26085, China), anti-Pink1 (Cohesion Biosciences, CPA5801, UK), anti-Parkin (Bioss, bs-23687R, China), anti-LC3A/LC3B (Santa Cruze, sc-398822, USA), anti-KIM-1 (Proteintech, 30948-1-AP, China), anti-NGAL (Affinity, DF6816, China), anti-GAPDH (Proteintech, 10494-1-AP, China), anti-β-actin (ABclonal, AC038, China), HRP-conjugated Goat anti-Rabbit IgG (H + L) (ABclonal, AS014, China), HRP-conjugated Goat anti-Mouse IgG (H + L) (ABclonal, AS003, China), Goat anti-Rabbit IgG (H + L) (Thermo Fischer Scientific, AlexaFluor®488, A32731). FITC-F4/80 (Biolegend, 123108, USA), PE/CF594-CD11b (Biolegend, 101256, USA), PE-CD86 (Biolegend, 105008, USA), PerCP/Cy5.5-CD206 (Biolegend, 141715, USA), Alexa Fluor® 700-CD45 (Biolegend, 147716, USA), FITC-Ly6G (Biolegend, 127606, USA) and Alexa Fluor® 700-CD11c (Biolegend, 117320, USA). Antibody dilutions were according to manufacturer's instructions.

2.2. *Preparation and characterization of SSNPs*

The extraction of the drug was carried out by the traditional method of heat reflux extraction in the ratio of 2:1 between *Scutellaria barbata* D. Don and *Scleromitrion Diffusum* (Willd.) R. J. Wang (SB−SD) (Tongrentang, Beijing, China), and then rotary evaporation with a rotary evaporator (Labconco) was used to obtain the preliminary aqueous extract, subsequently extracted with petroleum ether and saturated *n*-butanol twice respectively, The *n*-butanol fraction was put into the pretreated AB-8 resin column elution with 70% ethanol, The eluate was retained, rotary evaporated and freeze dried on a freeze dryer (Labconco) to obtain the active site, after lyophilization we found that the water

solubility was good and the SSNPs formed were stably dispersed in the aqueous solution. The morphology of SSNPs was characterized by TEM (JEM-1200EX, Tokyo, Japan). The size distribution and charge measurement of SSNPs were measured by dynamic light scattering (DLS; Brookhaven, USA.) in water (pH 7.4) and hydrochloric acid buffer (pH 2.4). SSNPs were suspended at 1 mg/mL in water with 10 min of bath sonication prior to testing.

2.3. *In situ TEM imaging process*

To observe the particle formation of SSNPs, we selected two monomer molecules with representative structures, scutellarin (STR) and geniposidic acid (GPA), which were first dissolved in anhydrous ethanol at a molar ratio of 1:1, and then diluted with water to obtain the SGNPs (STR and GPA nanoparticles). 50 nL SGNPs solution was injected into the liquid cell of a 20 nm thick SiNx window. After that, the liquid cells were sealed with epoxy and dried out. High-resolution TEM (HRTEM) images, high angle annular dark-field scanning transmission electron microscopy (HAADF-STEM) and the elemental mapping were conducted using a ThermoFisher Talos operated at 50 kV. A beam current density of about 6 $e^{-}/(Å^2 \cdot s)$ was used within the whole observation. A high sensitivity TVIPS CMOS camera was used for real-time imaging at low dose conditions, which allowed a time resolution of 5 frames per second.

2.4. *Self-assembly molecular dynamics simulation*

Molecular simulations were further used to certify the driving interactions during assembly process. First, scutellarin (STR) and geniposidic acid (GPA) monomer molecules are modeled using Pymol software[18], and then we use ORCA to optimize the structures at B3LYP/6-311G basis set[19]. Afterward, Packmol program[20] was applied to construct a mixture system in a certain ratio, specifically STR/GPA (15:15), which was calculated as mole ratio of experimental methods. The resp charge and electrostatic potential map was calculated by B3LYP/6-311G method. On this basis, antechamber program was used to construct the RESP charge parameters[21] of the two molecules, and all the molecular parameters were generated by GAFF2 force field[22]. The molecular dynamics simulations were carried out using Gromacs2018 program[23]. In brief, the side length of the water box was set to 1 nm using TIP3P water box model[24]. 5000 steps of energy minimization were performed, followed by the simulation of fix heavy atoms (force constant of 1000 kJ/mol·nm^2) under NVT and NPT, respectively, for 100 ps. Finally, a 50 ns balance simulation (without any restrictions) was generated. The cutoff radius was set to 1.0 nm, and the time step was set to 2 fs. The configurations were saved every 10 ps for subsequent analysis.

2.5. *Molecular simulation of the interaction of nanoparticles and protein*

Using Desmond 2021.1 Academic Version[25], molecular dynamics simulations were performed. The OPLS4 force field[26] was selected for both the starch and protein systems. The protein and starch were placed in a cubic water box. In the simulation, the cutoffs for electrostatic interactions and van der Waals interactions were both set to 1.0 nm, and the time step was set to 2 fs. The temperature was maintained at 30 °C, and the pressure at 1.01325 bar. The constructed system first underwent 100 ps of Brownian Dynamics NVT equilibration at 10 K, followed by 12 ps of NVT and 12 ps of NPT equilibration dynamics at 10 K. Subsequently, a 12 ps restrained NPT equilibration for heavy atoms and a 24 ps unrestrained NPT equilibration were performed. Finally, a 100 ns molecular dynamics sampling was conducted.

2.6. *Encapsulation and quantification of SSNPs protein corona*

Fresh intestinal tissues were isolated from mouse and rinsed with saline, the isolated SSNPs were instilled inside the intestinal tissues and ligated at both ends with surgical sutures, placed in a six-well plate with saline on a shaking table for 3 and 6 h. The supernatant at 3 and 6 h was first centrifuged at a low speed of $3000\times g$, and then the supernatant was further centrifuged at an ultracentrifugation speed of $100{,}000\times g$. The precipitates were collected after 2 h, and then added PBS to centrifuge twice at $100{,}000\times g$ to obtain SSNPs-col, which was then incubated with 50% whole blood (0.067 mol/L PBS) at 37 °C for 6 h, and then centrifuged at $1000\times g$, and then the supernatant was further centrifuged at an ultracentrifugation speed of $100{,}000\times g$. The precipitates were collected and washed twice with PBS by centrifugation to obtain SSNPs-col-blo finally. In corona desorption studies, upon the final wash, the pellet (SSNPs-col, SSNPs-col-blo) was dispersed in RIPA buffer (mixed with 1:100 protease inhibitor cocktail), was sonicated and then centrifuged at $10{,}000\times g$, 15 min, and the supernatant fraction obtained, was subjected to protein determination by microBCA assay. The remaining supernatant were stored at −80 °C before further analysis.

2.7. *SDS−PAGE*

SSNPs-col, blood, SSNPs-col-blo (15 μg) of lysate supernatant were mixed with loading buffer and incubated at 100 °C for 10 min. The samples were then loaded onto a 12% PAGE gel and run at 80 mV for 30 min and 120 mV for 1 h. For rapid silver staining, the gel was fixed in 100 mL fixing solution (50% methanol, 10% acetic acid, 50 μL formaldehyde) for 4 h, followed by washing with 30% ethanol and deionized water. The gel was then sensitized with silver dye sensitizer (1 ×) for 2 min and washed three times with deionized water. The gel was then impregnated with silver ion solution (1 ×) for 10 min. The gel was then washed with deionised water for 1 min and subjected to band development using 100 mL of silver staining solution for 10 min. After development, the reaction was stopped with silver staining termination solution (1 ×). The gel was digitally photographed against a white background.

2.8. *Protein corona digestion for mass spectrometry*

The obtained lysate supernatant (SSNPs-col-blo) was processed with 40 μg/mL protein, followed by the introduction of pre-cooled acetone for protein precipitation, then protein lysate to dissolve the precipitate, subsequent addition of an alkylating reductant, before incubating at 95 °C for 5 min. After the samples cooled down, protease was introduced, followed by a 2 h incubation of the blend at 37 °C. Insert a termination agent to halt the reaction following the enzyme digestion process. The specimen was introduced into the desalting column, followed by centrifugation using the peptide washing agents 1 and 2, respectively. Then transfer the desalting column to a fresh centrifugation tube, where the peptides are collected *via* centrifugation following the addition

of the peptide eluent. Conclusively, the samples underwent concentrating using a vacuum freeze-centrifuge concentrator, while the test samples were reconstituted using 0.1% (*v/v*) formic acid (diluted in UPLC−MS grade water) and added to iRT for on-line detection.

2.9. Cell culture and treatments

The human renal tubular epithelial cell line (HK-2) and mouse tubular epithelial cell line (TCMK-1) were purchased from American Type Culture Collection. The murine-derived macrophage cell line (RAW264.7) was purchased from BeNa Culture Collection. HK-2 cells were cultured in DMEM/F12 medium, TCMK-1 cells were cultured in DMEM/H medium, and RAW264.7 cells was cultured in RPMI 1640 medium, which was supplemented with 10% (*v/v*) fetal bovine serum (FBS) and 1% (*v/v*) penicillin/streptomycin at 37 °C, 5% CO_2 in a humidified incubator. For the *in vitro* experiments, HK-2 and TCMK-1 cells were pre-incubated with various concentrations of SSNPs for 4 h or Ferrostatin-1 (Fer-1, 5 μmol/L) for 1 h in the corresponding groups. And then, the cells were pre-treated with ML385 (5 μmol/L) for 1 h and indicated concentration of cisplatin (DDP) for 24 h.

2.10. Cellular uptake assay

SSNPs, SSNPs-col-blo, SSNPs-hb and SSNPs-BSA were labeled with FITC, and their particle concentrations were normalized to the initial drug concentration to ensure uniformity in the initial sample concentrations and fluorescence intensities across the same batch of samples. RAW264.7 cells and TCMK-1 cells (1×10^5) were treated with FITC-labelled SSNPs, SSNPs-col-blo, SSNPs-hb and SSNPs-BSA at equivalent fluorescent unit values and doses. After 2 h, the cells were collected for immunofluorescence analysis and flow cytometry analysis. For immunofluorescence staining, cells were fixed with 4% paraformaldehyde. Then the cytoskeleton was incubated with phalloidin (1 μg/mL), and the cell nucleus was stained with DAPI (1 mg/mL) for 5 min. Finally, the slides were sealed and observed under confocal microscope (Zeiss LSM980, Germany). For flow cytometry, cells were collected, washed and analyzed by flow cytometry (CytoFLEX, Beckman, USA).

2.11. Cell proliferation assay

HK-2 cell proliferation was assessed with CCK-8 assay according to the manufacturer's instructions. Briefly, cells were cultured at 37 °C in 96-well plate (1×10^4 cells/well/100 μL) for 24 h and then incubated with different concentrations of SSNPs or DDP. At 24 h time point, 10 μL of CCK-8 solution was added to each well and the plate was incubated for 1 h. The optical density (OD) at 450 nm was measured using a microplate reader (SpectraMax i3, Molecular Devices, USA).

2.12. Intracellular ROS and lipid peroxidation detection

Cells were collected and incubated with H2DCFDA (5 μmol/L) and C11-BODIPY$^{581/591}$ (1 μmol/L) for 30 min at 37 °C under dark conditions. After washing three times with PBS, the cells were detected by flow cytometry (Beckman Cytoflex). In addition, cell sections were incubated with H2DCFDA and C11-BODIPY$^{581/591}$ under the same conditions and intracellular ROS and lipid peroxidation levels were assessed using confocal microscopy (Zeiss LSM980, Germany).

2.13. Mitochondrial damage and membrane potential assessment ($\Delta\Psi m$)

To detect mitochondrial superoxide dismutase (mitochondrial ROS, mitoROS) and mitochondrial damage, cells were incubated in medium with MitoSOX™ Red (2.5 μmol/L) and Mitotracker™ green (5 μmol/L) for 30 min at 37 °C, and then were detected by flow cytometry (Beckman Cytoflex) or images were acquired on a confocal microscope (Zeiss LSM980, Germany). Mitochondrial membrane potential was assessed using JC-10 fluorescent dye staining employing fluorescence microscopy and flow cytometry following the manufacturer's guidelines (Biosharp, China). Briefly, cells were cultured according to the instructions and incubated with JC-10 (5 μg/mL) for 20 min at 37 °C. After washing twice with binding buffer, cells were detected by flow cytometry (Beckman Cytoflex). Data were analyzed by FlowJo software.

2.14. Iron content analysis

For cell Fe^{2+} quantification, they were placed in 6-well plates and incubated at 37 °C in a 5% CO_2 incubator, with the measurement of their iron ion levels conducted using the intracellular iron colorimetric test kit. The assay involves adding a single working reagent at 60 °C, followed by incubation for 1 h, then another with an iron ion reagent and incubating for 30 min at room temperature. After centrifuging the supernatant at 12,000 rpm for 5 min (Eppendorf 5424, Germany), it was gathered to assess the optical density at 520 nm.

2.15. Apoptosis analysis

Apoptosis was detected by flow cytometry and terminal deoxynucleotidyl transferase (TdT) dUTP nick end labelling (TUNEL) staining. Apoptosis analysis was performed using annexin V-PE/7-AAD staining and flow cytometry according to the manufacturer's instructions (Vazyme, Nanjing, China). Flow cytometry was detected by a Beckman Cytoflex instrument and data were analyzed by FlowJo software. Renal tissue apoptosis was detected by TUNEL assay using the *in situ* cell death assay manual. TUNEL-positive cells were detected with a fluorescence microscope (Nikon, Tokyo, Japan), and the average number of apoptotic cells was calculated by manually counting TUNEL-positive cells in six random fields of view (200 ×) in each group.

2.16. Animal experiments

Male C57BL/6 mice (6−8 weeks, 20−22 g) and *Nrf2*$^{-/-}$ mice (Nfe2l2, 8 weeks, 22−24g) were purchased from SiPeiFu (SPF) Biotechnology Co., Ltd. (Beijing, China) and Jackson Laboratories (Bar Harbor, USA), respectively. To evaluate the effects of SSNPs on DDP-induced acute injury (AKI), mice were randomly divided into the following six groups: Control group (saline), DDP group (20 mg/kg DDP), SSNPs-H group (28 g/kg SSNPs), DDP + SSNPs-L group (20 mg/kg DDP + 7 g/kg SSNPs), DDP + SSNPs-M group (20 mg/kg DDP + 14 g/kg SSNPs) and DDP + SSNPs-H group (20 mg/kg DDP + 28 g/kg SSNPs). Different doses of SSNPs were administrated intragastrically (i.g.) for 9 days, and DDP (20 mg/kg) was administrated

intraperitoneally (i.p.) on Day 7 to induce acute kidney injury. On Day 10, the mice were euthanized, and blood and kidney samples were collected for further analysis. The same method was applied to establish a folic acid (FA)-induced acute kidney injury model. The experimental groups were randomly divided into the following four groups: Control group (saline), SSNPs group (28 g/kg SSNPs) and FA group (250 mg/kg) and FA + SSNPs group (250 mg/kg FA + 28 g/kg SSNPs). All animal experiments were approved by the Institutional Animal Care and the Animal Ethics Committee of Dalian Medical University, Dalian, China (Approval No. AEE24045).

2.17. Biochemical and histological analysis

Blood urea nitrogen (BUN) and blood creatinine (CRE), which reflect the level of renal function, were assessed using commercial kits. For histological analysis, fresh kidney tissues were fixed and embedded in paraffin. Subsequently, the samples were cut into 4 μm thick slices for hematoxylin and eosin (H&E) and Periodic Acid-Schiff (PAS) staining. Furthermore, H&E and PAS sections were assigned scores according to the percentage of tubules that were damaged: 4 = 75%−100%, 3 = 51%−75%, 2 = 26%−50%, 1 = 1%−25%; 0 = normal.

2.18. Immunohistochemistry and immunofluorescence analysis

To conduct immunohistochemical tests, kidney tissue slices underwent an overnight incubation at 4 °C with primary antibodies targeting KIM-1 (HAVCR1, 1:100), NGAL (LCN2, 1:50), and 4-HNE (1:50), followed by further incubation using HRP-linked secondary antibodies. After DAPI staining for 10 min, the slices were observed under a light microscope (Olympus BX51, Japan). For immunofluorescence analysis, cell lines were collected and fixed in 4% paraformaldehyde, following which they were incubated with a primary Nrf2-targeting antibody (1:100) overnight at 4 °C. They were then exposed for 1 h to Alexa Fluor 488-linked goat anti-rabbit IgG (1:1000). Following DAPI staining for 5 min, the sections were sealed and observed under a fluorescence microscope (Nikon, Tokyo, Japan).

2.19. Flow cytometry analysis

Whole kidneys were collected on the tenth day, mechanically dissociated, digested, and the erythrocytes lysed to obtain a single-cell suspension of the kidney. Suspension cells were stained with antibodies against CD45, Ly6G, CD11b and CD11c (BioLegend), washed twice with FACS buffer, and then the cells were analyzed using a flow cytometer (CytoFLEX, Beckman, USA).

2.20. BMDM polarization detection

Bone marrow-derived macrophages (BMDMs) were isolated and cultured from mouse bone marrow. For polarization, BMDMs were pretreated with SSNPs (100 μg/mL) for 4 h. Afterward, the cells were treated with IFN-γ (20 ng/mL) and LPS (100 ng/mL) for 24 h to induce M1 polarization. During the experiment, the cells were first stained with antibodies against F4/80, CD11b and CD86 (BioLegend) for surface labeling. Next, the cells were treated with a permeabilization agent to allow nuclear staining. After permeabilization, the cells were stained with an anti-CD206 (BioLegend) antibody for nuclear labeling. Following the staining steps, the cells were analyzed using flow cytometry (Beckman CytoFLEX) to assess the expression levels of CD86 (M1 marker) and CD206 (M2 marker). All results were analyzed using FlowJo software.

2.21. Western blotting analysis

Cells and kidney tissue were collected and lysed on ice for 30 min before being disrupted by ultrasound for 2 min. Equal amounts of protein (20−40 μg) were separated by 10%−15% SDS-PAGE, and the separated proteins were transferred to a PVDF membrane and blocked with 5% skimmed milk powder in PBS buffer for 1 h at room temperature. The proteins were incubated overnight with antibodies against β-actin (1:5000), GAPDH (1:5000), GPX4 (1:1000), xCT (1:1000), PINK1 (1:1000), Parkin (1:1000), LC3 (1:200), Nrf2 (1:2000), HO-1 (1:1000) and NQO1 (1:3000), and then incubated with appropriate secondary antibodies and developed. The resulting images were analyzed using ImageJ software to determine the relative expression levels. Protein expression levels were normalized to β-actin or GAPDH.

2.22. Statistical analysis

The data are expressed as mean ± standard error of the mean (SEM). A P-value of less than 0.05 was considered statistically significant. The statistical analysis of differences between two unpaired groups was conducted using an unpaired two-tailed t-test. The data from the multiple groups were subjected to one-way analysis of variance (ANOVA), followed by post hoc tests. The statistical analysis was conducted using GraphPad Prism (GraphPad Software, San Diego, CA, USA, RRID: SCR_002798), a statistical software program. $*P < 0.05$, $**P < 0.01$, $***P < 0.001$, $****P < 0.0001$. ns, not significant. All sample sizes for statistical analyses were greater than or equal to 3 ($n \geq 3$).

3. Results

3.1. Characterisation and self-assembly mechanism of SSNPs

The extraction process employed a 2:1 ratio of *Scutellaria barbata* D. Don (SB) and *Scleromitrion Diffusum* (Willd.) R. J. Wang (SD). Using our previously established extraction method, we obtained aqueous extracts, and 70% ethanol elution fraction. To evaluate the antioxidant activity of these components, two standard assays were conducted: DPPH radical inhibition and superoxide anion scavenging activity. The results demonstrated that the 70% ethanol elution fraction exhibited superior antioxidant performance in both assays and was thus identified as the active fraction (Supporting Information Fig. S1). Unlike conventional aqueous extraction methods, the refined aqueous extraction employs a systematic fractionation approach that is grounded in the polarity of molecules. Upon redispersion in water, this fraction was found to exist stably in the form of nanoparticles, termed SSNPs (SB and SD nanoparticles), as shown in Fig. 1A. Transmission electron microscopy (TEM) images clearly demonstrated the uniform spherical structure of SSNPs (Fig. 1B), with a diameter of approximately 82.0 ± 11.9 nm. As illustrated in Fig. 1C, the hydrodynamic size analysis revealed that the particle size distribution of SSNPs was approximately 100.6 ± 7.4 nm, with a polydispersity index (PDI) of 0.215, indicating good dispersion. Furthermore, zeta potential of SSNPs was

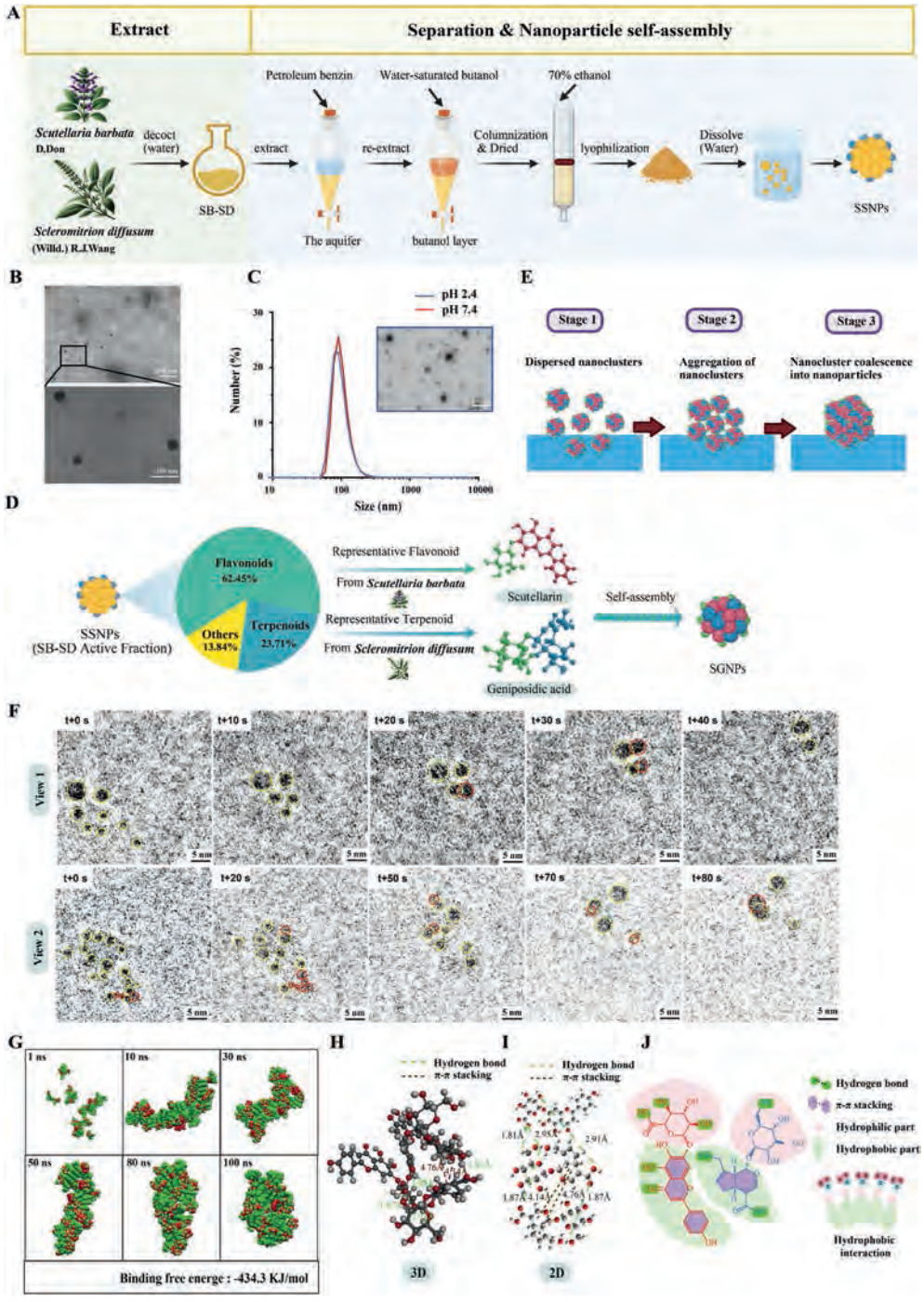

Figure 1 SB-SD formed self-assembled SSNPs during the extraction and isolation process. (A) Flow chart of SB−SD extraction and isolation of active ingredient with SSNPs formation. (B) Morphology of SSNPs under transmission electron microscope (TEM). (C) The size distribution of SSNPs under neutral (pH 7.4) and acidic (pH 2.4) conditions and the morphology under acidic conditions through transmission electron microscope (TEM). (D) Schematic diagram of the self-assembly of representative compounds STR and GPA in the active fraction of SSNPs to form SGNPs. (E) Schematic of the fusion of SGNPs. (F) *In situ* transmission electron microscopy (TEM) of SGNPs undergoing aggregation and fusion in aqueous solution. Scale bar: 5 nm. (G) Molecular dynamics simulation of self-assembly of STR and GPA from 0 to 100 ns. (The hydrophobic part in GPA and STR is shown as green, the glycosyl group as red). (H, I) 3D and 2D force structure diagrams of GPA and STR (Green dotted line indicates hydrophobic interactions. Brown dotted line indicates $\pi-\pi$ stacking). (J) Schematic representation of flavonoid and terpenoid self-assembly.

-15.6 ± 1.9 mV (Supporting Information Fig. S2). Additionally, under acidic conditions (pH = 2.4), SSNPs maintained a stable particle size distribution (86.6 ± 5.0 nm) and a low PDI value (0.261), demonstrating excellent acid resistance. This characteristic suggests that SSNPs can effectively resist gastric acid during oral administration, thereby enhancing the bioavailability and stability of the active fraction. We also observed the particle size distribution in simulated gastric fluid, simulated intestinal fluid, and serum, further confirming the stability of the particles (Supporting Information Fig. S3). These findings indicate potential self-assembly behavior of chemical components during the preparation process of the active fraction, and the particles exhibit good stability.

Ultra-high performance liquid chromatography/quadrupole time of flight mass spectrometry (UHPLC/QTOF−MS) analysis further revealed that the main components of the SB−SD active fraction were flavonoids (62.5%) and terpenoids (23.7%) (Fig. 1D, Supporting Information Figs. S4 and S5, Supporting Information Table S1). To elucidate the molecular assembly mechanism underlying the formation of nanoparticles in the active fraction, we selected scutellarin (STR), a prototypical flavonoid glycoside derived from SB, and geniposidic acid (GPA), a representative iridoid glycoside derived from SD, for conducting self-assembly simulations. As it is depicted in Fig. 1D−F, *in situ* liquid phase transmission electron microscopy (*in situ* TEM) observations reveal that during the solvent exchange process, STR and GPA undergo intermolecular interactions, leading to the spontaneous self-assembly and formation of STR-GPA nanoparticles (SGNPs). The aggregation of nanoparticles proceeds through three stages. In the initial stage, the two compounds form nanoclusters, which then aggregate due to intermolecular interactions, causing the distance between clusters to gradually decrease over time. During the second stage, preliminary fusion occurs among the particles, driven by non-covalent interactions, leading to an increase in the surface area of individual particles. Finally, in the third stage, the particles fully fuse, resulting in a reduction in particle count and the formation of larger, stable nanoparticles (Supporting Information Video S1).

Supplementary video related to this article can be found at https://doi.org/10.1016/j.apsb.2025.05.024

Molecular simulations are utilised to facilitate a more profound exploration of the molecular mechanisms that the self-assembly of STR and GPA. Specifically, the simulation involved the introduction of 15 STR molecules and 15 GPA molecules into a water container (Supporting Information Fig. S6). As shown in Fig. 1G, the two small molecular compounds were initially distributed as discrete particles. The process of aggregation occurred within 10 ns, and was characterized by the presence of hydrophilic glycosyl groups (indicated in red) located on the surface of the particles. As time progressed, the particles amalgamated closely. Supporting Information Videos S2 and S3 documented the active aggregation of particles. The formation of particles from STR and GPA through self-assembly has been attributed to the occurrence of intense interactions between molecules. In detail, the structures of STR and GPA are characterized by the participation of their fragrant configurations in $\pi-\pi$ layering interactions, while their glycosyl groups engage in hydrogen bonds. The comprehensive architectural details are illustrated in Fig. 1H and I. The stability of the system was verified through the root mean square deviation (RMSD) curve, leveling off around 30 ns. Additionally, the decrease in the solvent-accessible surface area (SASA) and the radius of gyration (RoG) post the first 25 ns confirms the trend of self-assembly (Supporting Information Fig. S7). 2-Phenylchromene forms the main progenitor nucleus of flavonoids. Typically, flavones are combined with sugars in the synthesis of glycosides. In this procedure, the carbonyl moiety has the ability to establish hydrogen bonds, and the benzene ring plays a key role in promoting the $\pi-\pi$ stacking interaction. The fundamental structural unit of terpenoids is isoprene. A hydrophobic backbone promotes hydrophobic bonding, allowing the hydrophilic hydroxyl and carboxyl groups to participate in the formation of hydrogen bonds[27]. Furthermore, hydrophobic nuclei and hydrophilic glycosides may additionally generate hydrophobic interactions. As a result, these components are capable of propelling the creation of self-assembled entities through hydrophobic connections and hydrogen bonds (Fig. 1J)[28]. In summary, the distinct structural features of these small molecules increased intermolecular forces, which in turn helped to form self-assembled nanoparticles.

Supplementary video related to this article can be found at https://doi.org/10.1016/j.apsb.2025.05.024

3.2. *Characterization of protein corona and biodistribution of SSNPs*

The mechanisms by which nanoparticles interact with biological systems, in particular the development of the protein corona, are crucial to understanding why nanoparticles function physiologically and have a fate in the body[29]. To this end, our research focused on how the protein corona forms on the surface of SSNPs when they interact with body fluids, and the resulting biological effects. As shown in Fig. 2A, we employed *ex vivo* murine intestine to introduce SSNPs into the luminal environment, with the objective of simulating the interaction between ingested nanoparticles and the intestinal environment. Subsequently, we gathered nanoparticles that effectively breached the intestinal physical barrier, termed as SSNPs-colon (SSNPs-col). Moreover, we co-incubated SSNPs-col with blood *in vitro* and collected the resulting particles, known as SSNPs-colon-blood (SSNPs-col-blo), thereby replicating the biological process by which nanoparticles penetrate the intestinal barrier and enter blood. As shown in Fig. 2B, the analysis of protein bands in SSNPs-col, blood, and SSNPs-col-blo reveals that these nanoparticles develop a protein corona on their surface (as marked by the blue arrow) post intestinal tissue penetration.

However, this protein decreases when mixed with blood, likely due to competitive binding occurring at specific sites. Consequently, in the corresponding bands, most of the proteins in SSNPs-col-blo are derived from the blood (indicated by the red arrow). We observed a significant increase in the zeta potential of the particles after the formation of the protein corona. Notably, the zeta potential of SSNPs-col-blo reached -29.7 ± 1.1 mV, indicating enhanced stability of the protein-coated nanoparticles (Fig. S2). Proteomic analysis was conducted on SSNPs-col-blo using liquid chromatography-mass spectrometry (LC−MS) (Supporting Information Table S2). The ten most abundant proteins are illustrated in Fig. 2C including haemoglobin, skeleton protein, anion exchange protein and albumin. Since skeleton proteins are ubiquitous in eukaryotic cells, anion-exchange proteins mainly regulate osmotic pressure and lack a unique functional significance. Therefore, albumin and hemoglobin were entered into our research scope. Albumin might be specifically

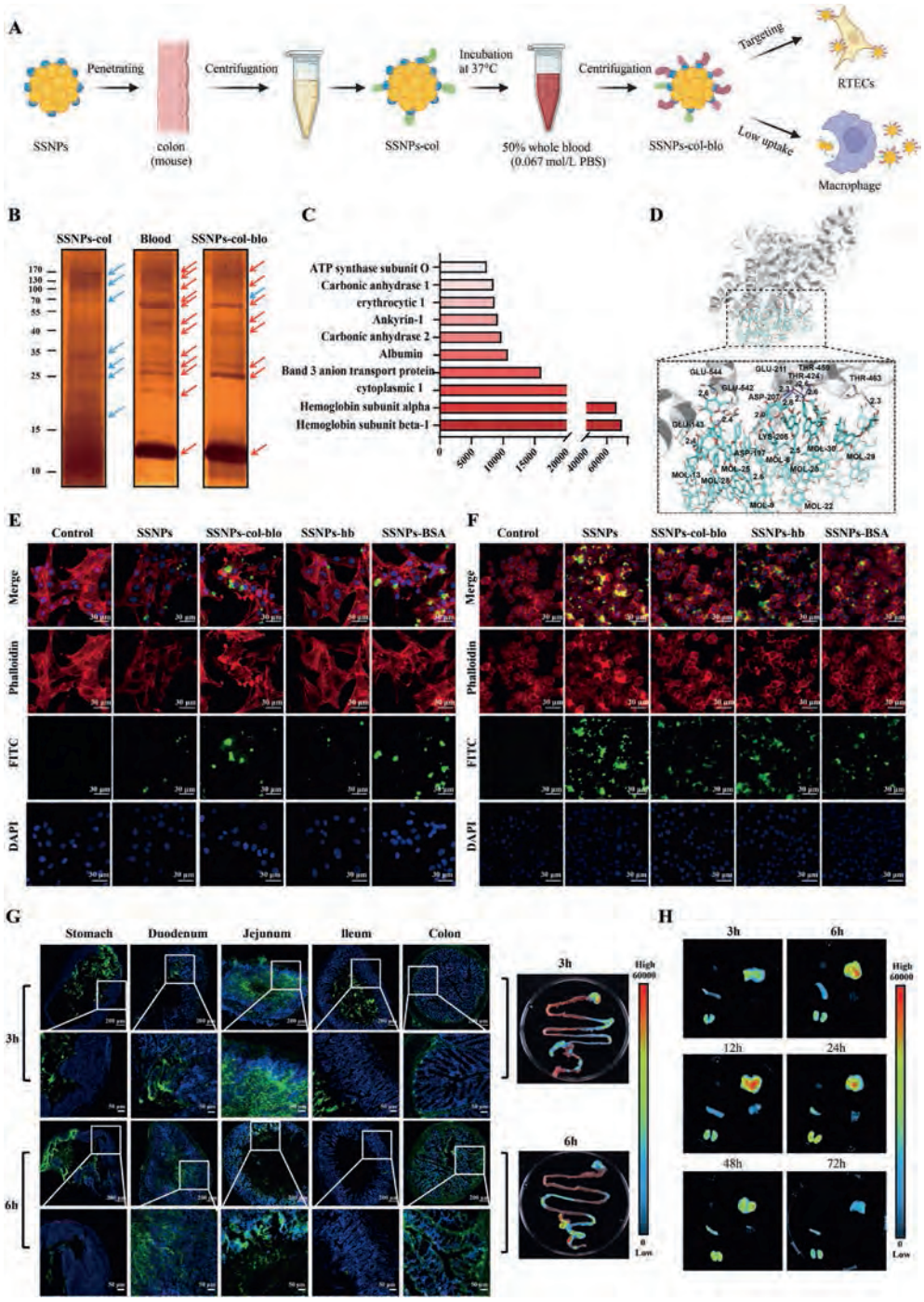

Figure 2 The protein composition analysis and renal targeting of SSNPs with protein corona. (A) Schematic diagram illustrating the *in vitro* simulation of particle construction with protein coronas to improve cellular uptake. (B) Typical silver staining of SSNPs-col and SSNPs-co-blo. Blood was used for the SSNPs-co-blo control. (C) Protein crown composition analysis diagram. (D) Molecular docking analysis of SSNPs binding to albumin. Representative immunofluorescence images of (E) TCMK-1 cells and (F) RAW264.7 cells treated with FITC-labelled SSNPs, SSNPs-col-blo, SSNPs-hb and SSNPs-BSA for 2 h. Scale bar: 30 μm. (G) After labelling SSNPs with FITC, the retention and uptake of nanoparticles in the intestine of C57BL/6 mice were observed by immunofluorescence and bioluminescence. Scale bar: up, 200 μm; down, 50 μm. (H) Representative bioluminescence images of main organs of C57BL/6 mice treated with FITC-labelled SSNPs at different times.

adsorbed with the presence of hydrophilic glycosylation sites on the surface of SSNPs.

To verify this hypothesis, molecular docking analysis between the sites exposed on the surface of SGNPs and albumin (Uniprot ID: P07724) was performed (Fig. 2D). For illustrative purposes, we specifically selected the unit fragments constituting the SGNPs, which encompassed the STR and GPA along with their corresponding structural sites. These structural sites were

systematically labeled as MOL1 to MOL30 (including GPA1−15 and STR16−30). The hydrogen bond binding sites were primarily located between the glycosyl groups of SGNPs and the amino acid residues of albumin (Supporting Information Fig. S8). Hydrogen bonds were identified between the small molecules and amino acid residues: MOL-13 and GLN-143, MOL-28 and GLU-544, MOL-25 and GLU-542, MOL-9 and ASP-197, MOL-22 and LYS-205, MOL-29 and THR-463, MOL-20 and GLU-211, MOL-30 and GLU-211, THR-459, GLU-424, as well as MOL-8 and GLU-424. In addition, we also found that the hydrophobic sites exposed by STR/GPA have hydrophobic interactions with albumin, which plays an important role in promoting their tight and stable binding. Hydrophobic interactions were observed between the following: MOL-3, MOL-13, MOL-12, MOL-24, MOL-18, MOL-22, MOL-17 within the particles and THR-203, PRO-541, GLU-143, GLY-423, CYS-201, LYS-205, and ASP-207 from albumin. The calculated binding free energy was −989.48 kcal/mol albumin. These findings collectively indicate that SGNPs exhibit a strong binding affinity with albumin. As illustrated in Supporting Information Fig. S9, the RMSD curves indicate that the protein and particles reached a relatively stable binding state after approximately 65 ns. RMSF shows that fluctuations were primarily localized at the amino acid residues and glycosyls, further confirming extensive interactions between the glycosyls on the particle surface and the protein (Supporting Information Fig. S10).

Previous studies have revealed that nanoparticles exhibit unique immune evasion and targeting properties by adsorb albumin and hemoglobin on their surfaces[30,31]. To investigate the uptake characteristics of SSNPS with different protein coronas on phagocytes and renal tubular epithelial cells, we incubated these particles *in vitro* with RAW264.7 cells and TCMK-1 cells. As shown in Fig. 2E, compared to SSNPs, TCMK-1 cells exhibited higher uptake efficiency for SSNPs-col-blo and SSNPs-BSA. Furthermore, it was observed that SSNPs-col-blo, SSNPs-hb, and SSNPs-BSA significantly reduced the uptake by RAW264.7 cells (Fig. 2F and Supporting Information Fig. S11). These results collectively suggest that the protein corona on the surface of SSNPs can effectively enhance the bioavailability in target tissues or organs while reducing nonspecific uptake. Furthermore, we investigated the absorption process of Cy5.5-labeled SSNPs within the digestive tract. As depicted in Figs. 2G and 3 h post-administration, the drug significantly accumulated in the jejunum, while colon epithelial cells also began to exhibit a certain degree of absorptive capacity. As time progressed to 6 h, the residual amount of SSNPs in the jejunum lumen decreased, indicating that most SSNPs had been effectively absorbed by colon epithelial cells. This finding is of great significance for understanding the absorption mechanisms of SSNPs in the gastrointestinal tract. The *in vivo* distribution study of Cy5.5-labeled SSNPs revealed that the drug remained in the liver for approximately 12 h and in the kidneys for up to 24 h post-administration (Fig. 2H). To further elucidate the specific distribution of the drug within the kidneys, we assessed the co-localization of the drug with both the glomerulus and renal tubules following drug labeling. Our findings indicated that, irrespective of whether in the renal medulla or renal cortex, the drug co-localized with the renal tubules (Supporting Information Fig. S12). This observation suggests that the drug may engage in active transport mechanisms, demonstrating a certain degree of targeting specificity for the renal tubules. Furthermore, over time, a reduction in drug content within the renal cortex was accompanied by an increase in the renal medulla, which provides further evidence that the drug is delivered to the kidneys *via* the bloodstream and subsequently migrates from the renal cortex to the renal medulla, thereby exerting its therapeutic effects on the renal tubules. This data provides a rationale for determining an appropriate dosing time window when constructing animal models of acute kidney injury in subsequent studies.

3.3. The protective efficiency of SSNPs in vivo

To evaluate the preventive effects of SSNPs *in vivo*, C57BL/6 mice were intraperitoneally (i.p.) injected with cisplatin (DDP) to induce AKI. As shown in Fig. 3A, the renal phenotype of mice in the model group exhibited clear signs of ischemia, kidney enlargement, and pallor. After administering different concentrations of SSNPs, these ischemic and pathological changes were reversed to varying degrees. Kidney injury modeling was performed according to the animal model described in the methods (Fig. 3B), and the obtained serum and kidney tissues were evaluated for damage. The renal injury in mice was assessed, and as illustrated in Fig. 3C−E, SSNPs can significantly reverse DDP-induced increases in kidney index, serum urea nitrogen, and creatinine levels. To examine the levels of lipid peroxidation, malondialdehyde (MDA) and reduced glutathione (GSH) were measured in the serum of mice. It was found that different concentrations of SSNPs reversed the production of MDA and the depletion of GSH induced by DDP to varying degrees (Fig. 3F and G). As illustrated in Fig. 3H, the results of H&E and PAS staining demonstrated that the renal tubules exhibited severe dilatation (red arrow), evident oedema (blue arrow) and cast formation (black arrow) of renal tubular epithelial cells in the model group. As illustrated in Fig. 3I and J, the defensive role of SSNPs in preventing renal damage caused by DDP was confirmed through H&E and PAS coloration results. Post SSNPs treatment, the kidney injury showed a substantial improvement. Additionally, treatment with DDP led to increased amounts of kidney injury molecule-1 (KIM-1) and NGAL, but these were reduced after SSNPs treatment. The TUNEL stain indicated a notable rise in apoptosis in tissues treated with DDP, a trend which SSNPs successfully counteracted. The quantitative results of IHC and TUNEL staining are shown in Supporting Information Fig. S13. The treatment's advantages were further evidenced in a model of folic acid (FA)-induced acute renal injury in mice, offering more proof of the treatment's effectiveness (Supporting Information Fig. S14). We further assessed the safety of the drug by conducting additional liver function tests and histopathological analysis of liver tissue. The levels of alanine aminotransferase (ALT) and aspartate aminotransferase (AST) remained within the normal range, indicating that liver function remained normal following treatment. H&E staining revealed preserved liver architecture, with hepatocytes arranged in a regular pattern, and no indications of inflammation, damage, or fibrosis. These findings provided further evidence that SSNPs do not induce liver toxicity (Supporting Information Fig. S15). As illustrated in Supporting Information Fig. S16, in the study of kidney single-cell suspensions from the DDP-stimulated AKI model, flow cytometry showed that SSNPs treatment markedly decreased neutrophil accumulation, thus reducing the infiltration of inflammation. Furthermore, our research explored the *in vitro* polarization aspects of BMDMs (Supporting Information Fig. S17) and discovered that SSNPs enhance M2 polarization and lessen M1 polarization. This suggests that SSNPs amplify anti-inflammatory macrophages and diminish pro-inflammatory macrophages, resulting in potent anti-inflammatory actions.

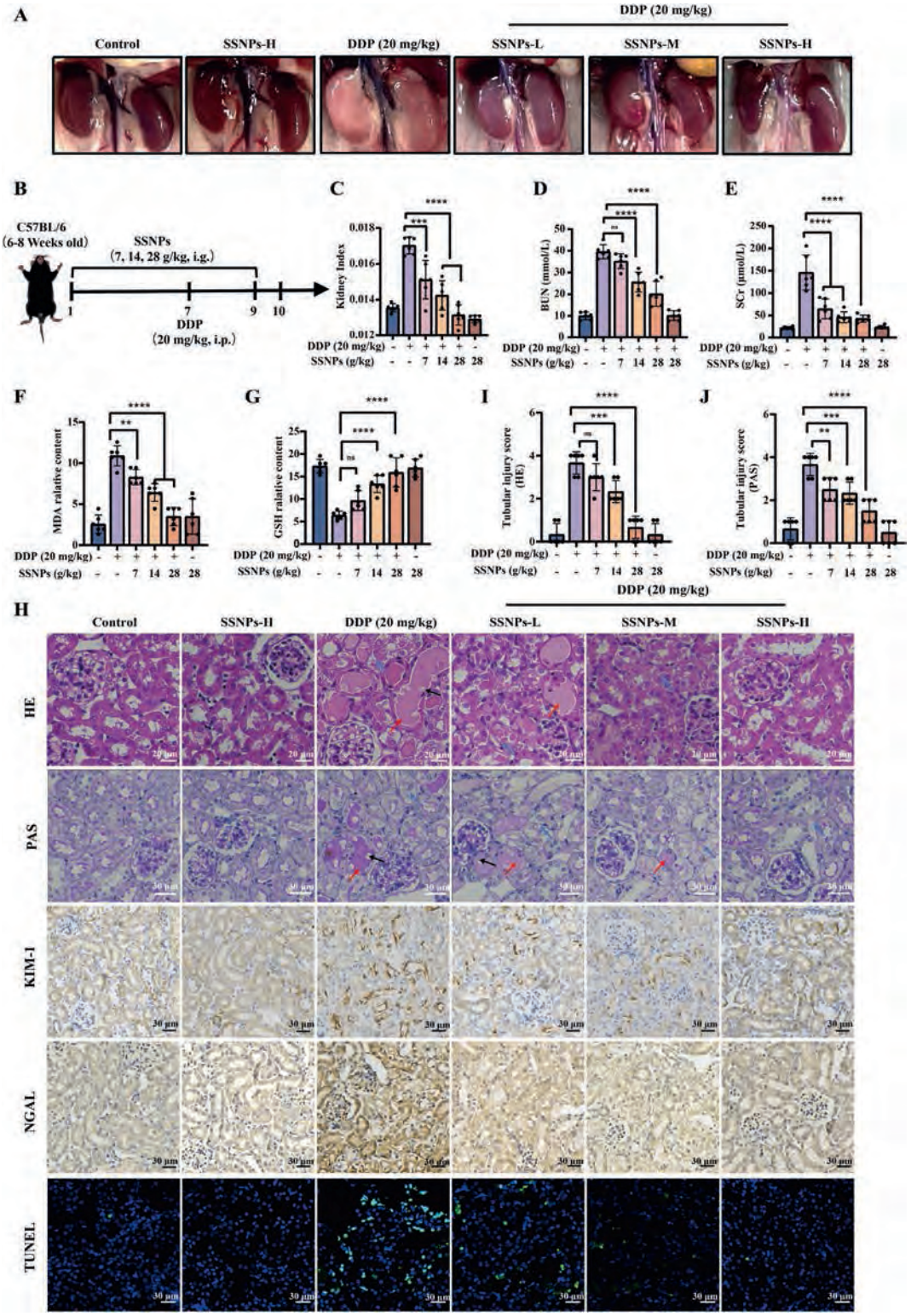

Figure 3 SSNPs alleviated cisplatin (DDP)-induced acute kidney injury in C57BL/6 mice. (A) The representative photographs of mice kidney from six groups. (B) Schematic diagram of mice AKI model. (C) The renal index of mice from six groups. The serum levels of (D) BUN and (E) SCr in mice from six groups. Serum levels of (F) MDA and (G) GSH in mice from six groups. (H) H&E staining showed evidence of renal tissue damage, while PAS staining indicated the presence of renal lesions characterised by glycogen deposition. Immunohistochemistry for KIM-1 and NGAL was performed to assess the extent of renal lesions. TUNEL immunofluorescence staining was used to detect the degree of apoptosis in different subgroups. Scale bar: 20 or 30 μm. (I) H&E and (J) PAS staining scores. Each point represents the mean ± SEM ($n = 6$). $^{*}P < 0.05$, $^{**}P < 0.01$, $^{***}P < 0.005$, $^{****}P < 0.0001$. ns, no significance.

3.4. Potent antioxidation effects of SSNPs in vitro

HK-2 cells were treated with varying doses of DDP and SSNPs in order to ascertain the optimal concentrations for the inhibition and promotion of cell growth. As illustrated in Fig. 4A and B, DDP demonstrated a dose-dependent inhibitory effect on cell viability, whereas SSNPs exhibited a dose-dependent promotion of cell growth. It is noteworthy that SSNPs treatment markedly attenuated the impact of DDP on cell death (Fig. 4C). Similar results were observed in TCMK-1 cells (Supporting Information Fig. S18). Nrf2, a key regulator of the antioxidant response, is known to alleviate oxidative stress by activating downstream antioxidant pathways[32]. To further investigate the regulatory effects of SSNPS on oxidative stress, we examined the expression levels of key oxidative stress-related proteins. As depicted in Fig. 4D−J, SSNPs markedly upregulated the expression of Nrf2, HO-1, and NQO1, even in the presence of DDP. Furthermore, immunofluorescence staining revealed that DDP reduced the expression of Nrf2 protein in HK-2 cells, while SSNPs effectively restored Nrf2 protein levels (Fig. 4K). These results were confirmed in TCMK-1 cells, further supporting the validity of our observations (Supporting Information Fig. S19). The quantification of ROS by H2DCFDA staining (Supporting Information Fig. S20) and flow cytometry demonstrated that ROS levels were elevated in HK-2 cells after DDP treatment, as illustrated in Fig. 4L and M. To further validate this conclusion, similar results were obtained in TCMK-1 cells (Supporting Information Fig. S21). As oxidative stress promotes the accumulation of ROS, which in turn triggers apoptosis, we further examined the impact of SSNPs on DDP-induced apoptosis. DDP-induced apoptosis was significantly attenuated by SSNPs (Fig. 4N and O), suggesting that the protective mechanism of SSNPs may involve the regulation of oxidative stress pathways.

3.5. SSNPs protected renal tubular epithelial cells from DDP-induced ferroptosis

Free iron can interact with ROS to form lipid-free radicals, which can rapidly react with oxygen and induce lipid peroxidation. As previously demonstrated, SSNPs are capable of reducing the accumulation of ROS (LipROS) induced by DDP. To gain further insight into the quantitative analysis of ferric ions, a ferric ion detection kit was employed to quantify the ferric ion content in the supernatant of HK-2 cells lysate. The results demonstrated that SSNPs treatment can reduce intracellular accumulation of ferric ions caused by DDP in different cells (Fig. 5A and B, Supporting Information Fig. S22). As illustrated in Fig. 5C and D, SSNPs were observed to reverse the MDA production and GSH depletion induced by DDP. Subsequently, the regulatory effect of SSNPs on the expression of iron death-related target genes was further assessed. DDP treatment resulted in a significant reduction in the expression of GPX4 and xCT, which could be dose-dependently increased by SSNPs (Fig. 5E). The statistical results are provided in Supporting Information (Supporting Information Fig. S23). As shown in Fig. 5F, SSNPs were found to reverse the DDP-induced increase in 4-HNE for fluorescence staining of mouse kidney tissue. The quantitative results are shown in Supporting Information Fig. S24. Ferroptosis, which was defined as a novel non-apoptotic pathway of cell death characterized by iron-mediated excessive lipid peroxidation. Furthermore, previous study reported that DDP-induced renal tubular epithelial cell ferroptosis through ROS/HO-1/GPX4 axis[33]. We thus evaluated the level of LipROS in TCMK-1 cells and HK-2 cells (Fig. 5G−I, Supporting Information Figs. S25 and S26). Compared with control, SSNPs and Fer-1 could effectively reverse the increase of LipROS induced by DDP. Furthermore, electron microscopy results (Fig. 5J) show that, as indicated by the red arrows, mitochondria were significantly shrunk and deformed following DDP treatment. In contrast, SSNPs treatment improved mitochondrial morphology, with clearer mitochondrial cristae, as indicated by the blue arrows. Taken together, our results suggest that SSNPs can mitigate the DDP-induced ferroptosis in renal tubular epithelial cells.

3.6. SSNPs attenuated mitochondrial damage and promoted mitophagy in vitro and in vivo

As DDP is capable of boosting mitochondrial ROS production in mouse renal tubular epithelial cells (mRTECs)[34], we viewed mitochondrial ROS production in TCMK-1 cells using MitoSOX fluorescent probe. As illustrated in Fig. 6A and B, SSNPs, as well as Fer-1 (a ferroptotic inhibitor), decreased mitochondrial ROS generation in response to DDP. These results were confirmed in HK-2 cells, further supporting the validity of our observations (Supporting Information Fig. S27). To investigate the total number and overall health of mitochondria in TCMK-1 cells, we stained cellular mitochondria with MitoTracker Green and MitoTracker Red, which stain all the mitochondria and mitochondria with intact membrane potential, respectively. The findings indicated that SSNPs and Fer-1 significantly ameliorated DDP-induced mitochondrial damage (Fig. 6C and D), and effectively reversed the DDP-induced reduction in mitochondrial numbers (Supporting Information Fig. S28). We assessed the effects of DDP treatment on mitochondrial function in TCMK-1 cells using JC-10 fluorescence detection and flow cytometry. DDP treatment led to an increased green fluorescence intensity ratio of JC-10 (Supporting Information Fig. S29), indicating a significant reduction in mitochondrial membrane potential ($\Delta\Psi_m$) following DDP exposure. Nonetheless, the administration of SSNPs and Fer-1 effectively reversed the loss of $\Delta\Psi_m$ (Fig. 6E and F). Evaluating the accumulation of mitochondrial ROS in damaged mitochondria involved conducting immunofluorescence tests using MitoTracker Green co-located with MitoSOX Red. The results indicate that SSNPs and Fer-1 reversed the rise in mitochondrial ROS linked to mitochondrial damage caused by DDP (Fig. 6G). For a deeper exploration into how SSNPs regulate mitophagy, we assessed the protein expressions related to it. As it is depicted in Fig. 6H and I, SSNPs significantly upregulated the expressions of PINK1, Parkin, and LC3 in a dose-dependent manner, indicating the promotion of mitophagy. Moreover, transmission electron microscopy (Fig. 6J) revealed that mitochondria in renal tubular epithelial cells of mouse kidney tissue treated with DDP exhibited unclear morphology and cristae, with swollen mitochondrial vacuoles, as indicated by the red arrows. In contrast, treatment with SSNPs restored the normal shape and cristae of the mitochondria, as indicated by the blue arrows, and also revealed fragmented mitochondria surrounded by double-membrane structures, as indicated by the green arrows, indicating of mitophagy. Collectively, these findings indicate a strong connection between SSNPs' defense against nephrotoxicity caused by DDP and the activation of mitophagy.

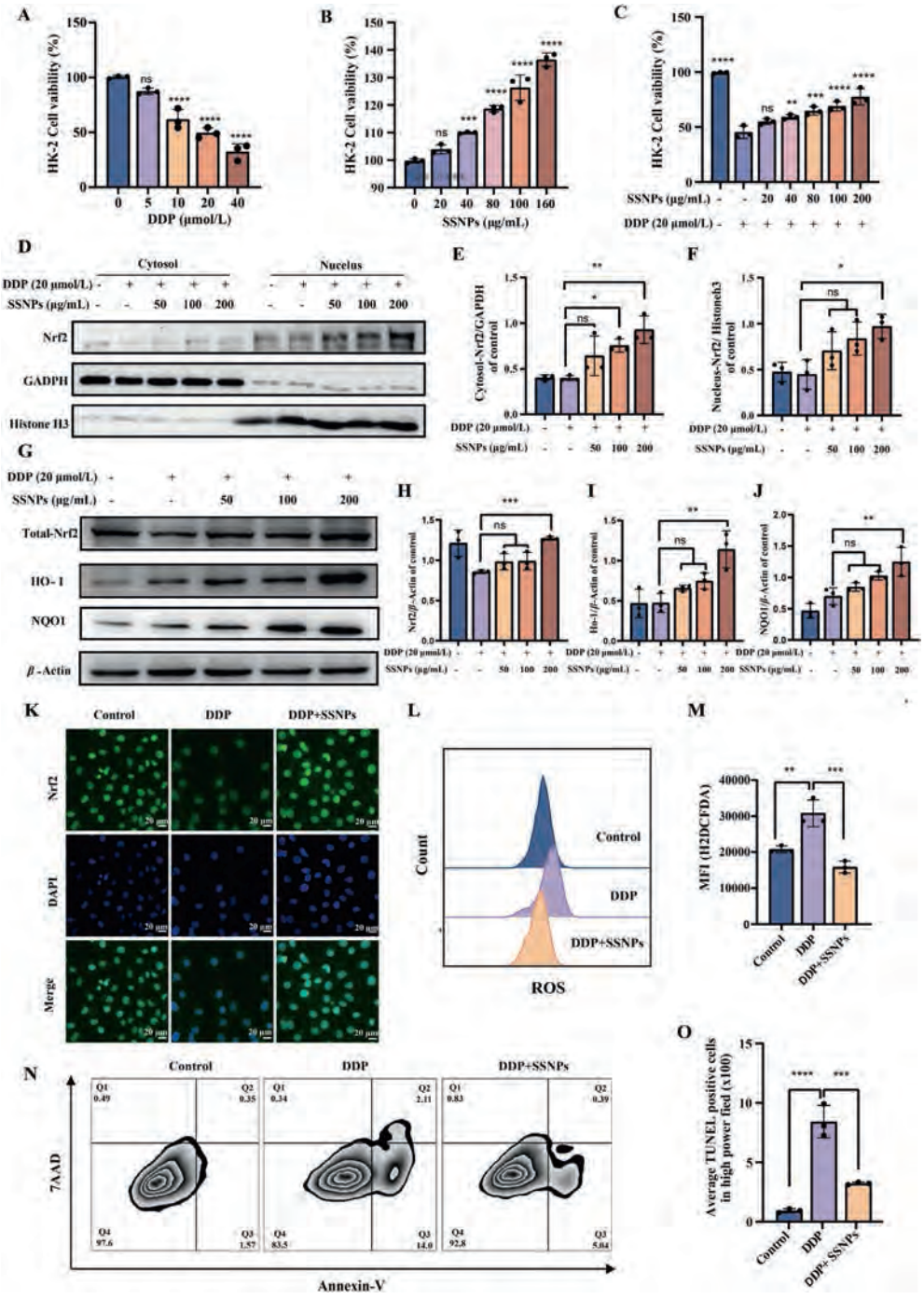

Figure 4 SSNPs mitigated DDP-induced oxidative stress in HK-2 cells. Proliferations of HK-2 cells treated with different concentrations of (A) DDP and (B) SSNPs for 24 h were measured by CCK8 assay. (C) Proliferations of HK-2 cells pretreated with different concentrations of SSNPs for 4 h, and then treated with or without DDP (20 μmol/L) for 24 h were measured by CCK8 assay. (D) Immunoblots of cytosol-/nucelus-Nrf2 in HK-2 cells and quantitative analysis of (E) cytosol-Nrf2 and (F) nucelus-Nrf2. (G) Immunoblots of total-Nrf2, HO-1 and NQO1 in HK-2 cells and quantitative analysis of (H) total-Nrf2, (I) HO-1 and (J) NQO1. (K) Representative fluorescence images showing the expressions of Nrf2 in HK-2 cells. Scale bar: 20 μm. Flow cytometry histograms (L) and quantification (M) of ROS level in HK-2 cells treated with DDP (20 μmol/L), SSNPs (200 μg/mL). Representative flow cytometry zebra plots (N) and the quantification (O) of apoptotic cells in TCMK-1 cells pretreated with treated SSNPs (200 μg/mL) for 4 h, and then treated with DDP (40 μmol/L) and for 24 h. Each point represents the mean ± SEM ($n = 3$). $^{*}P < 0.05$, $^{**}P < 0.01$, $^{***}P < 0.005$, $^{****}P < 0.0001$. ns, no significance.

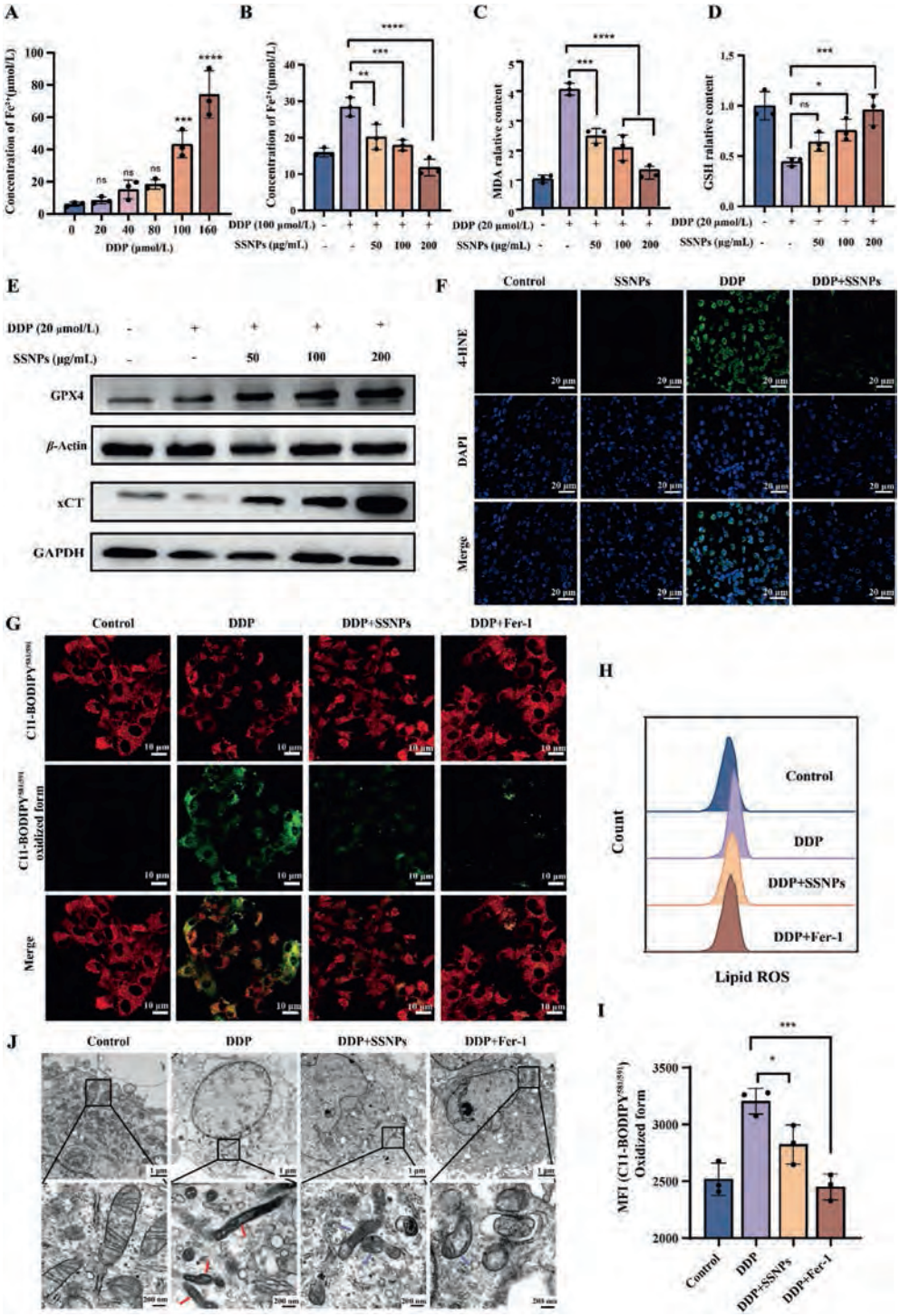

Figure 5 The effect of SSNPs on alleviating DDP-induced ferroptosis. (A) The levels of Fe^{2+} in HK-2 cells treated with different concentrations of DDP for 24 h. (B) The levels of Fe^{2+} in HK-2 cells pre-treated with different concentrations of SSNPs for 4 h and then treated with DDP (100 μmol/L) for 24 h. (C) The levels of MDA production and (D) GSH depletion in HK-2 cells pre-treated with different concentrations of SSNPs for 4 h and then treated with DDP (20 μmol/L) for 24 h. (E) The protein levels of GPX4 and xCT in HK-2 cells were analyzed by Western blotting. (F) Representative fluorescence images showing the levels of 4-HNE in kidney tissues from DDP-induced AKI mice. Scale bar: 20 μm. (G) Representative fluorescence images showing the induction of ferroptosis in TCMK-1 cells pre-treated SSNPs (200 μg/mL) for 4 h or Fer-1 (5 μmol/L) for 1 h and then treated with DDP (40 μmol/L) for 24 h. The cells were stained with C11-BODIPY$^{581/591}$. Scale bar: 10 μm. Representative flow cytometry histograms (H) and the quantification (I) of lipid ROS level in TCMK-1 cells. (J) Transmission electron microscopy images of TCMK-1 cells. Red arrows (damaged mitochondria), blue arrows (recovering mitochondria). Scale bar: up, 1 μm; down, 200 nm. Each point represents the mean ± SEM ($n = 3$). *$P < 0.05$, **$P < 0.01$, ***$P < 0.005$, ****$P < 0.0001$. ns, no significance.

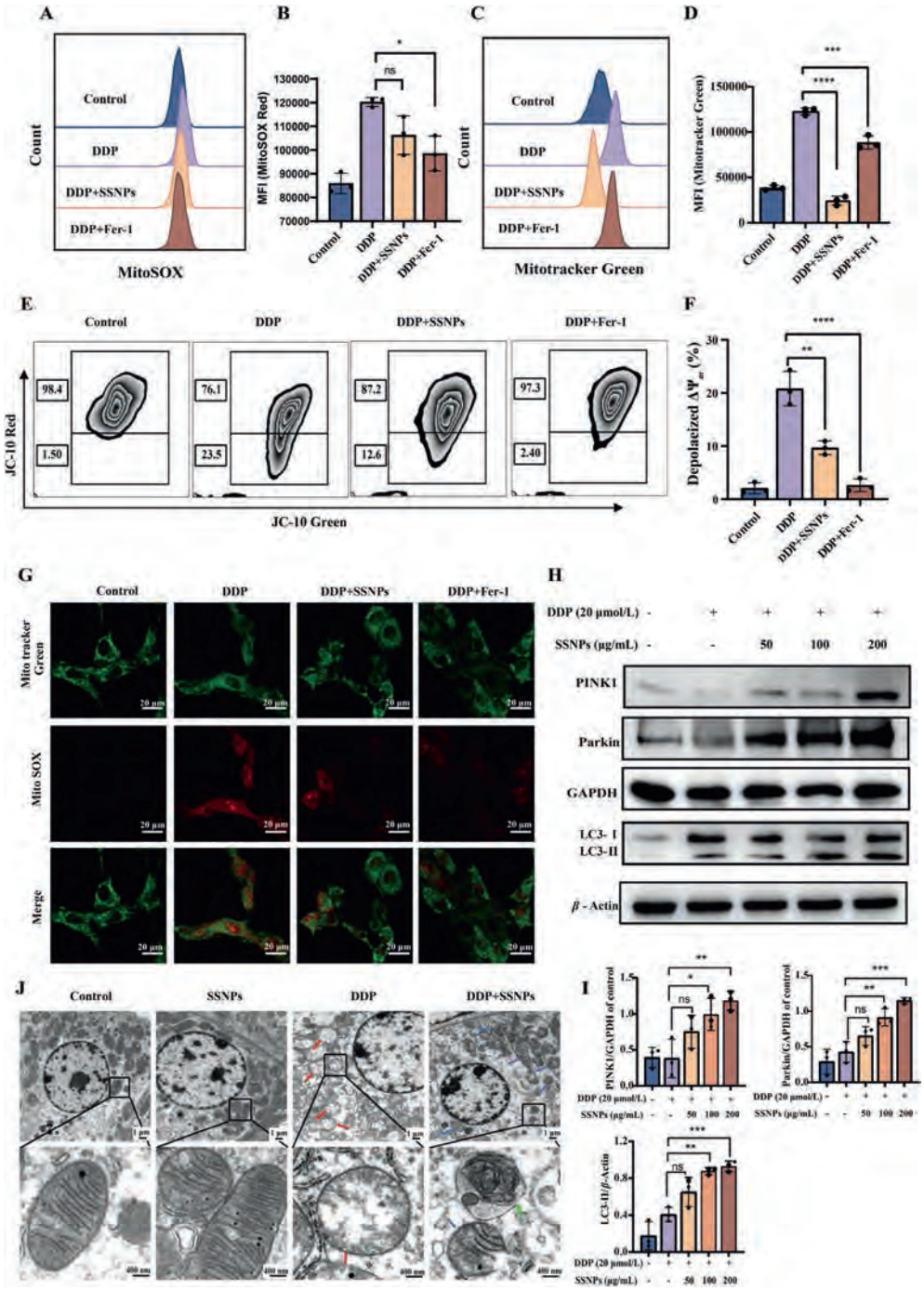

Figure 6 SSNPs alleviated DDP-induced mitochondrial damage and enhanced mitophagy. (A, B) The levels of mitochondrial ROS in TCMK-1 cells were detected by flow cytometry with the fluorescent probe MitoSOX. (C, D) The levels of mitochondrial damage in TCMK-1 cells were determined by flow cytometry with the fluorescent probe MitoTracker Green. (E, F) The levels of mitochondrial membrane potential in TCMK-1 cells were detected by flow cytometry with the fluorescent probe JC-10. (G) The immunofluorescence assay was used to assess the accumulation of mitochondrial ROS in damaged mitochondria with MitoTracker Green and MitoSOX. Scale bar: 20 μm. (H, I) The protein levels of PINK1, Parkin and LC3 in TCMK-1 cells were detected by Western blotting. (J) Transmission electron microscopy images in renal tubular epithelial cells of mice kidney tissues. Red arrows (damaged mitochondria), blue arrows (recovering mitochondria), green arrows (mitophagy). Scale bar: up, 1 μm; down, 400 nm. Each point represents the mean ± SEM ($n = 3$). *$P < 0.05$, **$P < 0.01$, ***$P < 0.005$, ****$P < 0.0001$. ns, no significance.

3.7. The powerful protective efficiency of SSNPs through Nrf2 pathway in vitro and in vivo

Nrf2 is a well-known key regulator of the antioxidant response element (ARE) and plays a critical role in mitigating oxidative stress[35]. To determine whether the protective mechanism of SSNPs depends on Nrf2 in kidney, both an Nrf2 inhibitor (ML385) and *Nrf2*$^{-/-}$ mice were used to verify the effects *in vitro* and *in vivo*. As illustrated in Fig. 7A, the SSNPs treatment reduced DDP-induced mitochondrial ROS production in TCMK-1 cells. However, this effect was significantly attenuated upon the addition of ML385. To quantify mitochondria, MitoTracker Red staining and flow cytometry were performed in TCMK-1 cells. The results demonstrated that the protective effect of SSNPs on mitochondria was diminished in the presence of ML385 (Fig. 7B). As shown in Fig. 7C, DDP-induced ROS accumulation was effectively suppressed by SSNPs, whereas this protective effect was attenuated following the addition of ML385, indicating the ability of SSNPs in alleviating oxidative stress was reduced. Similarly, as depicted in Fig. 7D, the protective effect of SSNPs against lipid peroxidation in TCMK-1 cells was also weakened in the presence of ML385. Additionally, western blot analysis was performed to assess the expression of Nrf2 and its related proteins following SSNPs and ML385 application in the model of TCMK-1 cellular damage induced by DDP. It can be seen that DDP could reduce the expression of Nrf2, HO-1 and GPX4, while ML385 could significantly reverse the increased expression of Nrf2, NQO1, HO-1 and GPX4 caused by SSNPs (Fig. 7E−I). For a deeper analysis of SSNPs' impact dependent on Nrf2, the study employed *Nrf2*$^{-/-}$ mice to develop a model for acute kidney injury (Fig. 7J). The relevant renal protection evaluation results (Supporting Information Fig. S30) show that the nephroprotective effect of SSNPs is significantly diminished in the *Nrf2*$^{-/-}$ mice. Electron microscopy revealed that the protective effect of SSNPs on mitochondrial morphology in *Nrf2*$^{-/-}$ mice was diminished (Fig. 7K). Following DDP treatment, mitochondria exhibited significant shrinkage and deformation, and no significant improvement in mitochondrial morphology was observed after SSNPs administration. Moreover, the study evaluated the protein manifestation of Nrf2 along with its associated proteins within the kidney tissues of *Nrf2*$^{-/-}$ mice. The findings showed a substantial reduction in the expression of Nrf2, NQO1, HO-1, and GPX4 (Fig. 7L). The research confirmed the vital function of Nrf2 in protecting SSNPs from DDP-induced oxidative stress, ferroptosis and mitochondrial damage.

4. Discussion

In the present study, we have created an innovative kind of self-assembly herbal nanoparticles (SSNPs) derived from *Scutellaria barbata* D. Don and *Scleromitrion diffusum* (Willd.) R. J. Wang, an effective counteragent for DDP and folic acid-triggered AKI. The SSNPs synthesized mainly consist of flavonoids and terpenoids, which are meticulously self-assembled to create nanostructures with outstanding solubility and dispersibility in water. In addition, the self-assembled SSNPs naturally adsorb albumin and hemoglobin following oral administration, forming a protein nanocorona. This process diminishes macrophage phagocytes and improves the absorption by renal tubular epithelial cells, thereby improving the absorption rate of SSNPs. This study reveals how flavonoids and terpenoids in SSNPs self-assemble *via* intermolecular forces like hydrogen bonds and $\pi-\pi$ interactions, and further underscores how these nanoparticles effectively protect the proximal tubular epithelial cells from oxidative stress and ferroptosis by activating the Nrf2 signaling pathway.

Traditional techniques for the extraction of SB−SD active components rely on aqueous extraction[36]. Here, we have developed a nano-TCM approach, where the fabrication of SSNPs involved a comprehensive refinement of conventional extraction techniques. By meticulously coordinating a series of steps involving extraction and self-assembly procedures, we accomplished the generation of stable nanoparticles. The sophisticated optimization process significantly improved both the uniformity and the purity of the derived components and their efficiency. These augmented interactions served as a pivotal cornerstone, underpinning the formation and stabilization of SSNPs. This method demonstrates the potential collaborative effect of nanotechnology and classical Chinese medicine, paving the way for the creation of innovative drugs with improved qualities and increased efficacy.

The herb pair SB−SD has garnered considerable attention due to their rich pharmacological activities and broad clinical application value[37]. Based on network-pharmacology and bioinformatics, analysis and comparison of the bioactive constituents indicated that SB−SD contained many components, some of which exert anti-tumor effects through diverse mechanisms like anti-oxidative, anti-inflammatory, pro-apoptotic, anti-angiogenic, and immune-regulating pathways[11,38]. However, the intricate make-up and compositions of these substances have resulted in a partial comprehension of their pharmacological dynamics. Previous study reported that SB−SD could induces ferroptosis in ovarian cancer cells (A2780, SKOV3 and OVCAR3) by promoting heme catabolism and ferritinophagy. Furthermore, administering SB−SD triggered increased levels of HO-1 and Nrf2 in three cell lines[11,38]. Our findings now show that the stable self-assembled nanoparticles (SSNPs) derived from SB−SD clearly inhibited DDP-triggered ferroptosis in renal tubular epithelial cells by reducing oxidative stress *via* Nrf2 enhancement. We speculate that this discrepancy may be attributed to two potential reasons. Firstly, the majority of TCM are a collection of multiple chemical components capable of exerting multiple therapeutic effects. In addition, this discrepancy may be attributed to the idiosyncratic nature of the cancer cel lines and proximal tubular epithelial cells utilized in these studies, as different cell lines can exhibit distinct behaviors and responses to various agents.

The findings from this study highlight the strong antioxidant activity of SSNPs and their potential protective effects against DDP-induced acute kidney injury (AKI). The data suggest that Nrf2 plays a central role in mediating these effects. In fact, as a significant regulator of redox balance, mounting evidence demonstrated that the use of Nrf2-activated agents can efficiently reduce ROS levels, thereby preventing or delaying the progression of various types of AKI[39,40]. In DDP-associated AKI, a common therapeutic tactic is to elevate the cellular antioxidant response to combat increased ROS. Previous studies indicated that Nrf2 knockout mice were more susceptible to DDP induction than wild-type mice. Pretreatment with CDDO-Im[41], an activator of Nrf2, prevented DDP toxicity in Nrf2 wild-type mice but not in Nrf2-deficient mice. Similarly, another Nrf2 inducer, melatonin[42], attenuated DDP-induced AKI probably by regulating Nrf2/HO-1 signaling. Consistently, our current study confirmed the nephroprotective effects of SSNPs against AKI *via* the Nrf2/HO-1 signaling pathway. Notably, when the Nrf2 inhibitor ML385 or Nrf2 knockout mice were used, the protective effects of SSNPs

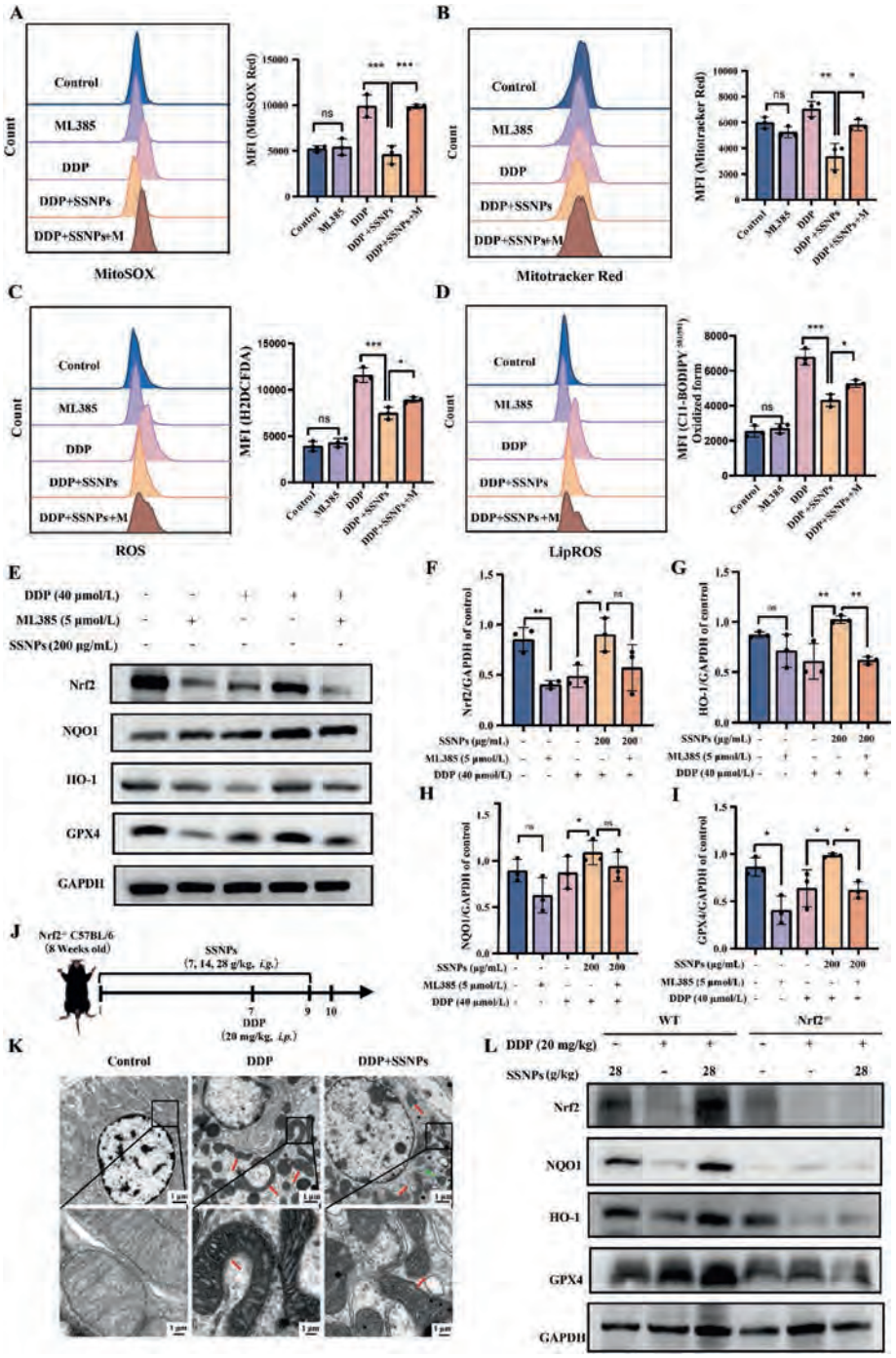

Figure 7 SSNPs attenuated DDP-induced oxidative stress, ferroptosis, and mitochondrial damage *via* the Nrf2 pathway. TCMK-1 cells were pre-treated with or without the Nrf2 inhibitor ML385 (5 μmol/L) for 1 h and SSNPs (200 μg/mL) for 4 h, and then treated with DDP (40 μmol/L) for 24 h (DDP + SSNPs + M: 40 μmol/L DDP, 200 μg/mL SSNPs and 5 μmol/L ML385). (A) The levels of mitochondrial ROS in TCMK-1 cells were detected by flow cytometry with the fluorescent probe MitoSOX. (B) The levels of mitochondrial damage in TCMK-1 cells were determined by flow cytometry with the fluorescent probe MitoTracker Red. (C) The ROS levels of TCMK-1 cells were detected by flow cytometry with the fluorescent probe H2DCFDA. (D) The lipid ROS levels of TCMK-1 cells were detected by flow cytometry with the fluorescent probe C11-BODIPY$^{581/591}$. (E) The protein levels of Nrf2, NQO1, HO-1, and GPX4 in TCMK-1 cells were detected by Western blotting and quantitative analysis of (F) Nrf2, (G) HO-1, (H) NQO1 and (I) GPX4. (J) Schematic representation of the therapeutic strategy using different concentrations of SSNPs for 20 mg/kg DDP challenge in *Nrf2*$^{-/-}$ mice. (K) Transmission electron microscopy images in renal tubular epithelial cells of *Nrf2*$^{-/-}$ mice kidney tissues. Red arrows (damaged mitochondria), green arrows (mitophagy). Scale bar: up, 1 μm. (L) The protein levels of Nrf2, NQO1, HO-1, and GPX4 in mice kidney tissues were detected by Western blotting. Each point represents the mean ± SEM ($n = 3$). *$P < 0.05$, **$P < 0.01$, ***$P < 0.005$, ****$P < 0.0001$. ns, no significance.

were significantly reduced, both *in vitro* and *in vivo*. These results strongly suggest that the protective effects of SSNPs are mediated through the activation of Nrf2 and its downstream antioxidant pathways. We further revealed that SSNPs might promote PINK1/Parkin-mediated mitophagy, thereby facilitating the clearance of damaged mitochondria and preventing excessive ROS accumulation. In addition, SSNPs exhibited the ability to lower intracellular iron levels, reduce lipid peroxidation and ultimately inhibit DDP-induced ferroptotic cell death. Overall, these findings provide a mechanistic basis for the use of SSNPs in mitigating DDP-induced AKI, emphasizing the critical role of Nrf2 activation and the regulation of ferroptosis in their protective effects.

Compared to conventional AKI treatments, nanotechnology-based therapeutics for AKI exhibited substantial and immense potential of further development[43]. Various nanotechnology-based therapeutic approaches including nanozymes, ROS scavenger nanomaterials loaded with antioxidants and anti-inflammatory agents have been designed to achieve an optimal therapeutic index by simultaneously improving both efficacy and safety. Likewise, in order to overcome the inherent limitations of TCM such as poor water solubility and low bioavailability, nanotechnology has been extensively explored for characteristics and therapeutic efficacy of nano-TCM[44,45]. Currently, the development of carrier-free nanomedicines of single active ingredients has partially overlooked the compatibility of TCM formulas. Utilizing multiple active ingredients through various nanostructures formed by self-assembly of TCM is a more potential strategy[46]. Recent researchers have found that the varied structures of herbal components facilitate their ability to self-assemble, enabling them to assemble with other molecules[46]. Common ingredients of TCM with self-assembly properties include terpenoids, quinones and glycosides. Tan et al.[47] exploited the intermolecular recognition properties of various ginsenoside monomers to facilitate the self-assembly of carrier-free ginsenoside nano-micelles gallic acid and resveratrol, both natural polyphenolic small molecules, are capable of co-assembling to form a two-component hydrogel[48].

In our study, in order to gain a deeper understanding of how SSNPs are produced, we analyzed their main components and selected two key compounds, scutellarin (STR) and geniposidic acid (GPA), to study their self-assembly mechanism. Observations showed that the process of nanoparticle aggregation proceeds in three stages. Initially, the duo of substances resulted in many tiny nanoparticles. With time, interactions between molecules decreased the separation between these nanoparticles, aiding in their clustering. In the latter phase, initial fusion took place among the nanoparticles *via* non-covalent interactions. During the ultimate phase, the nanoparticles experienced additional merging, diminishing their total quantity while creating stable structures. Molecular simulations have been employed to provide further mechanistic insights into the fusion process, thus highlighting the critical role of hydrogen bonding and $\pi-\pi$ stacking interactions in the initial association of the two compounds. These interactions promoted particle aggregation and fusion, ultimately resulting in the formation of stable nanoparticles. Collectively, these findings present a novel strategy and method for fostering research and development in nano-TCM.

Additionally, the formation of a protein corona is a crucial phenomenon in the interaction of nanoparticles with biological systems. Upon introduction into serum, nanoparticles swiftly adsorb proteins onto their surfaces, resulting in the establishment of a protein corona. This corona plays a significant role in determining the biological identity of the nanoparticles and influences their subsequent interactions with cells and tissues[49]. Previous studies have demonstrated that the hemoglobin-encapsulated nanodrug delivery system effectively evaded the immune system, which exhibiting significant targeting capabilities in cancer immunotherapy[30]. Also, Albumin coating boosts immune evasion and drug delivery by prolonging circulation time and allowing tumor targeting[31]. Consistently, protein corona-loading validation revealed that both albumin and hemoglobin reduced uptake of the nanoparticles by macrophages. Meanwhile, albumin was shown to enhance uptake by renal tubular epithelial cells, thereby conferring kidney-targeting properties to the nanoparticles. The formation of the protein corona further enhances our understanding of the transport, distribution, and metabolic processes of SSNPs *in vivo*, providing a solid theoretical basis for their application in biomedical research. Through molecular simulation techniques, we further confirmed the binding ability of glycosyl ligands exposed on the surface of SSNPs to albumin in the bloodstream, providing a solid theoretical basis for the formation of the protein corona on SSNPs. These findings highlight the potential of SB−SD-derived nanoparticles to achieve targeted drug delivery, minimize off-target effects, and enhance therapeutic efficacy, particularly in kidney-related applications.

Despite substantial advancements in our understanding of the specific renoprotective effects and underlying mechanisms of SSNPs, due to the compositional complexity and complicated mechanism, there remains gaps in our understanding. Future studies can further confirm the potent single active ingredients and take on the in-depth mechanism. Moreover, our study found that SSNPs can also accumulate in the liver, although no drug-related toxic effects were observed during the study, it is imperative to investigate the potential adverse effects or the potential protective effect on liver injury associated with the utilization of SSNPs. We anticipate broader use of our SSNPs in other oxidative stress-related diseases. Ultimately, we preliminarily elucidated the possible mechanism of self-assembly process of SSNPs *via* driven by hydrogen bonding and $\pi-\pi$ stacking interactions. The adaptability of the principle for the application of nano-TCM has not been substantiated through specific experimental verification. Future research endeavors will be undertaken.

5. Conclusions

This study proposes a pioneering approach in the domain of traditional Chinese medicine (TCM) by forming self-assembled herbal nanoparticles (SSNPs). The SSNPs, which contain flavonoids and terpenoids, have excellent water solubility and dispersion and are ideal for treating AKI. Through our extensive research, we revealed the complex process of self-assembly in these nanoparticles, driven by intermolecular dynamics like hydrogen bonds and $\pi-\pi$ interactions. The process of self-assembly has been shown to stabilize and purify nanoparticles, thereby protecting tubular epithelial cells from oxidative stress and ferroptosis by activating the Nrf2 signaling pathway. Further analysis revealed that SSNPs naturally absorb albumin and hemoglobin *in vivo*, leading to the creation of protein corona which improves bioavailability and kidney targeting. In summary, our present study clarifies the specific renoprotective effects and underlying mechanisms of SB and SD, and also establishes an innovative nano-TCM methodology for advancing traditional Chinese medicine and naturally occurring nanomedicines.

Acknowledgments

The study was supported by the National Natural Science Foundation of China (Nos. 81873195, 32471458, and 82473933), the Applied Basic Research Program of Liaoning Province (No. 2023JH2/101300103, China), the Liaoning Revitalization Talents Program (No. XLYC1907113, China), Chongqing Talents Program (cstc2022ycjh-bgzxm0111, China), the Natural Science Foundation of Chongqing, China (cstc2020jcyj-msxmX0411), Science and Technology Research Program of Chongqing Municipal Education Commission (KJZD-K202312802, China), the Distinguished Young Scholars in Dalian (2022RJ19, China). We would like to thank Shenzhen Shuli Tech Co., Ltd. for technical support for the molecular simulations. Scheme 1, Fig. 1A, D, 1E and Fig. 2A in this work were created using BioRender.

Author contributions

Lunyue Xia performed the majority of the experimental work. Qunfang Yang, Yutong Yang, Kaiyue Ding performed the *in vivo* experiments. Lanfang Zhang, Yunong Li, Borong Zhu, Liang Sun performed the *in vitro* experiment. Kangzhe Fu, Yijie Huo, Yuexue Huo, Peiyu Li performed experiments related to the extraction and analysis of drugs. Lunyue Xia and Qunfang Yang wrote the manuscript. Ya Liu, Haigang Zhang conceived the idea. Lin Zhang, Wenjun Shan, Liu Tao conceived the idea, designed the experiments, supervised the project and revised the manuscript.

Conflicts of interest

The authors have no conflicts of interest to declare.

Appendix A. Supporting information

Supporting information to this article can be found online at https://doi.org/10.1016/j.apsb.2025.05.024.

References

1. Kellum JA, Romagnani P, Ashuntantang G, Ronco C, Zarbock A, Anders HJ. Acute kidney injury. *Nat Rev Dis Primers* 2021;**7**:52.
2. Birkelo BC, Pannu N, Siew ED. Overview of diagnostic criteria and epidemiology of acute kidney injury and acute kidney disease in the critically ill patient. *Clin J Am Soc Nephrol* 2022;**17**:717−35.
3. He W, Ding C, Lin T, Wang B, Wang W, Deng Z, et al. An enzyme-mimicking reactive oxygen species scavenger targeting oxidative stress-inflammation cycle ameliorates IR-AKI by inhibiting pyruvate dehydrogenase kinase 4. *Theranostics* 2024;**14**:7534−53.
4. Xin W, Zhou J, Peng Y, Gong S, Liao W, Wang Y, et al. SREBP1c-mediated transcriptional repression of YME1L1 contributes to acute kidney injury by inducing mitochondrial dysfunction in tubular epithelial cells. *Adv Sci (Weinh)* 2025;**12**:e2412233.
5. Chen Q, Yang Y, Ying X, Huang C, Chen J, Wang J, et al. Hierarchical targeting nanodrug with holistic DNA protection for effective treatment of acute kidney injury. *Adv Sci (Weinh)* 2025;**12**:e2411254.
6. Zhang J, Ren X, Nie Z, You Y, Zhu Y, Chen H, et al. Dual-responsive renal injury cells targeting nanoparticles for vitamin E delivery to treat ischemia reperfusion-induced acute kidney injury. *J Nanobiotechnol* 2024;**22**:626.
7. Shu G, Wang C, Song A, Zheng Z, Zheng S, Song Y, et al. Water extract of earthworms mitigates kidney injury triggered by oxidative stress *via* activating intrarenal Sirt1/Nrf2 cascade and ameliorating mitochondrial damage. *J Ethnopharmacol* 2024;**335**:118648.
8. Qi Y, Zheng J, Zi Y, Song W, Chen X, Cao S, et al. Loureirin C improves mitochondrial function by promoting NRF2 nuclear translocation to attenuate oxidative damage caused by renal ischemia-reperfusion injury. *Int Immunopharmacol* 2024;**138**:112596.
9. Guo S, Zhou L, Liu X, Gao L, Li Y, Wu Y. Baicalein alleviates cisplatin-induced acute kidney injury by inhibiting ALOX12-dependent ferroptosis. *Phytomedicine* 2024;**130**:155757.
10. Ren Y, Wu F, Huo L, Wang X, Zhang Y, Fan M, et al. Switchable ROS generator and scavenger to prevent the cisplatin induced acute kidney injury and improve efficacy *via* synergistic chemodynamic/immune therapy. *Mater Today Bio* 2024;**29**:101328.
11. Wang Z, Liu M, Li GX, Zhang L, Ding KY, Li SQ, et al. A herbal pair of *Scutellaria barbata* D. Don and *Scleromitrion diffusum* (Willd.) R. J. Wang induced ferroptosis in ovarian cancer A2780 cells *via* inducing heme catabolism and ferritinophagy. *J Integr Med* 2024;**22**:665−82.
12. Pan Y, Ma T, Chen D, Wang Y, Peng Y, Lu T, et al. *Scutellaria barbata* D. Don and *Scleromitrion diffusum* (Willd.) R. J. Wang inhibits the progression of triple negative breast cancer though the activation inhibition of NF-κB triggered by CAFs-derived IL6. *J Ethnopharmacol* 2024;**335**:118656.
13. Zhang YL, Wang YL, Yan K, Deng QQ, Li FZ, Liang XJ, et al. Nanostructures in Chinese herbal medicines (CHMs) for potential therapy. *Nanoscale Horiz* 2023;**8**:976−90.
14. Zhang YL, Wang YL, Yan K, Li H, Zhang X, Essola JM, et al. Traditional Chinese medicine formulae QY305 reducing cutaneous adverse reaction and diarrhea by its nanostructure. *Adv Sci (Weinh)* 2024;**11**:e2306140.
15. Zhao B, Zhang Y, Fan Z, Lin Z, Wang L, Li H, et al. Study on the nanoaggregate formation mechanism and antipyretic effect of Maxing Shigan Decoction. *ACS Omega* 2024;**9**:19311−9.
16. Nie W, Liu Y, Lan J, Li T, He Y, Li Z, et al. Self-assembled nanoparticles from Xie-Bai-San Decoction: isolation, characterization and enhancing oral bioavailability. *Int J Nanomed* 2024;**19**:3405−21.
17. Li L, Cui H, Li T, Qi J, Chen H, Gao F, et al. Synergistic effect of berberine-based Chinese medicine assembled nanostructures on diarrhea-predominant irritable bowel syndrome *in vivo*. *Front Pharmacol* 2020;**11**:1210.
18. DeLano WL. Pymol: an open-source molecular graphics tool. *CCP4 Newsl Protein Crystallogr* 2002;**40**:82−92.
19. Neese F. The ORCA program system. *Wiley Interdiscip Rev Comput Mol Sci* 2012;**2**:73−8.
20. Martínez L, Andrade R, Birgin EG, Martínez JM. PACKMOL: a package for building initial configurations for molecular dynamics simulations. *J Comput Chem* 2009;**30**:2157−64.
21. Bayly CI, Cieplak P, Cornell W, Kollman PA. A well-behaved electrostatic potential based method using charge restraints for deriving atomic charges: the RESP model. *J Phys Chem* 1993;**97**:10269−80.
22. Wang J, Wolf RM, Caldwell JW, Kollman PA, Case DA. Development and testing of a general amber force field. *J Comput Chem* 2004;**25**:1157−74.
23. Van Der Spoel D, Lindahl E, Hess B, Groenhof G, Mark AE, Berendsen HJ. GROMACS: fast, flexible, and free. *J Comput Chem* 2005;**26**:1701−18.
24. Mark P, Nilsson L. Structure and dynamics of the TIP3P, SPC, and SPC/E water models at 298 K. *J Phys Chem A* 2001;**105**:9954−60.
25. Bowers KJ, Chow E, Xu H, Dror RO, Eastwood MP, Gregersen BA, et al. Scalable algorithms for molecular dynamics simulations on commodity clusters. In: *Proceedings of the 2006 ACM/IEEE conference on supercomputing*; 2006.
26. Lu C, Wu C, Ghoreishi D, Chen W, Wang L, Damm W, et al. OPLS4: improving force field accuracy on challenging regimes of chemical space. *J Chem Theor Comput* 2021;**17**:4291−300.
27. Li Q, Lianghao Y, Shijie G, Zhiyi W, Yuanting T, Cong C, et al. Self-assembled nanodrug delivery systems for anti-cancer drugs from traditional Chinese medicine. *Biomater Sci* 2024;**12**:1662−92.
28. Wang YL, Mu Y, Zhang YL, Luo X, Peng T, Tan Y, et al. Accessible and effective nanomedicines: self-assembly products from Chinese herbal medicines (CHMs). *Adv Funct Mater* 2024;**35**:2416151.

29. Li S, Cortez-Jugo C, Ju Y, Caruso F. Approaching two decades: biomolecular coronas and bio-nano interactions. *ACS Nano* 2024;**18**:33257−63.
30. Chen W, Tang C, Chen G, Li J, Li N, Zhang H, et al. Boosting checkpoint immunotherapy with biomimetic nanodrug delivery systems. *Adv Healthcare Mater* 2024;**13**:e2304284.
31. Hassanin I, Elzoghby A. Albumin-based nanoparticles: a promising strategy to overcome cancer drug resistance. *Cancer Drug Resist* 2020;**3**:930−46.
32. Bian Y, Dong J, Zhou Z, Zhou H, Xu Y, Zhang Q, et al. The spatiotemporal and paradoxical roles of NRF2 in renal toxicity and kidney diseases. *Redox Biol* 2024;**79**:103476.
33. Lin Q, Li S, Jin H, Cai H, Zhu X, Yang Y, et al. Mitophagy alleviates cisplatin-induced renal tubular epithelial cell ferroptosis through ROS/HO-1/GPX4 axis. *Int J Biol Sci* 2023;**19**:1192−210.
34. Yu B, Jin L, Yao X, Zhang Y, Zhang G, Wang F, et al. TRPM2 protects against cisplatin-induced acute kidney injury and mitochondrial dysfunction *via* modulating autophagy. *Theranostics* 2023;**13**:4356−75.
35. Liang NN, Guo YY, Zhang XY, Ren YH, He YZ, Liu ZB, et al. Mitochondrial dysfunction-evoked DHODH acetylation is involved in renal cell ferroptosis during cisplatin-induced acute kidney injury. *Adv Sci (Weinh)* 2024;**11**:e2404753.
36. Huang ST, Chen Y, Chang WC, Chen HF, Lai HC, Lin YC, et al. *Scutellaria barbata* D. Don inhibits the main proteases (M^{pro} and TMPRSS2) of severe acute respiratory syndrome coronavirus 2 (SARS-CoV-2) infection. *Viruses* 2021;**13**:826.
37. Ye CL, Huang Q. Extraction of polysaccharides from herbal *Scutellaria barbata* D. Don (Ban-Zhi-Lian) and their antioxidant activity. *Carbohydr Polym* 2012;**89**:1131−7.
38. Sui X, Gao B, Zhang L, Wang Y, Ma J, Wu X, et al. *Scutellaria barbata* D. Don and *Hedyotis diffusa Willd* herb pair combined with cisplatin synergistically inhibits ovarian cancer progression through modulating oxidative stress *via* NRF2−FTH1 autophagic degradation pathway. *J Ovarian Res* 2024;**17**:246.
39. Huang J, Zhao Y, Luo X, Luo Y, Ji J, Li J, et al. Dexmedetomidine inhibits ferroptosis and attenuates sepsis-induced acute kidney injury *via* activating the Nrf2/SLC7A11/FSP1/CoQ10 pathway. *Redox Rep* 2024;**29**:2430929.
40. Zheng Q, Xing J, Li X, Tang X, Zhang D. PRDM16 suppresses ferroptosis to protect against sepsis-associated acute kidney injury by targeting the NRF2/GPX4 axis. *Redox Biol* 2024;**78**:103417.
41. Liu M, Reddy NM, Higbee EM, Potteti HR, Noel S, Racusen L, et al. The Nrf2 triterpenoid activator, CDDO-imidazolide, protects kidneys from ischemia−reperfusion injury in mice. *Kidney Int* 2014;**85**:134−41.
42. Kilic U, Kilic E, Tuzcu Z, Tuzcu M, Ozercan IH, Yilmaz O, et al. Melatonin suppresses cisplatin-induced nephrotoxicity *via* activation of Nrf-2/HO-1 pathway. *Nutr Metab* 2013;**10**:7.
43. Ba X, Ye T, Shang H, Tong Y, Huang Q, He Y, et al. Recent advances in nanomaterials for the treatment of acute kidney injury. *ACS Appl Mater Interfaces* 2024;**16**:12117−48.
44. Patra JK, Das G, Fraceto LF, Campos EVR, Rodriguez-Torres MDP, Acosta-Torres LS, et al. Nano based drug delivery systems: recent developments and future prospects. *J Nanobiotechnol* 2018;**16**:71.
45. Zhang YB, Wang JF, Wang MX, Peng J, Kong XD, Tian J. Nano-based drug delivery systems for active ingredients from traditional Chinese medicine: harnessing the power of nanotechnology. *Front Pharmacol* 2024;**15**:1405252.
46. Guo X, Luo W, Wu L, Zhang L, Chen Y, Li T, et al. Natural products from herbal medicine self-assemble into advanced bioactive materials. *Adv Sci (Weinh)* 2024;**11**:e2403388.
47. Tan XR, Chao L, Feng KK, Le JQ, Shen JW, Shao JW. Self-assembled micelles of the natural medicine ginsenosides for cancer metastasis therapy. *J Ind Eng Chem* 2022;**116**:303−9.
48. Wang XC, Huang HB, Gong W, He WY, Li X, Xu Y, et al. Resveratrol triggered the quick self-assembly of gallic acid into therapeutic hydrogels for healing of bacterially infected wounds. *Biomacromolecules* 2022;**23**:1680−92.
49. Francia V, Yang K, Deville S, Reker-Smit C, Nelissen I, Salvati A. Corona composition can affect the mechanisms cells use to internalize nanoparticles. *ACS Nano* 2019;**13**:11107−21.